PERFORMANCE ASSESSMENT OF DIRECT DISPLACEMENT-BASED DESIGN

A Dissertation Submitted in Partial Fulfilment of the Requirements
for the Master Degree in

Earthquake Engineering and Engineering Seismology

By

Luke van der Burg

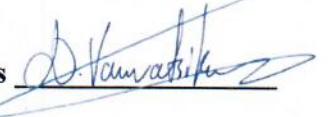Supervisors: Prof. Paolo Bazzurro & Prof. Dimitrios Vamvatsikos

February 2019

Istituto Universitario di Studi Superiori di Pavia

The dissertation entitled "Performance Assessment of Direct Displacement-Based Design", by Luke van der Burg, has been approved in partial fulfilment of the requirements for the Master Degree in Earthquake Engineering.

Prof. Paolo Bazzurro

Prof. Dimitrios Vamvatsikos

ABSTRACT

The performance of the innovative design procedure known as Direct Displacement-Based Design (DDBD) was assessed in terms of its ability to alleviate the computational burden of the pure performance-based seismic design (PBSD) methods. The study was limited to a single, completely regular, reinforced concrete cantilever wall building; designed to be suitable for three high seismicity sites located in Athens, Perugia and Focsani. Probability theory was used to fully characterise the maximum inter-storey drift ratio risk at the three sites by employing the Pacific Earthquake Engineering Research Center PBSD methodology. The seismic hazard was linked to the structural response with the conditioning intensity measure of Sa_{ave}, used to quantify the severity of earthquake-induced ground motions. Site-specific hazard assessment was performed using traditional probabilistic seismic hazard analysis (PSHA) to quantify the occurrence of the conditioning intensity measure. Hazard disaggregation was performed at ten intensity levels to facilitate hazard consistent record selection to represent the conditional mean and dispersion of spectral acceleration using the exact conditional spectra method. Fragility functions were estimated with analytical data collected from 200 ground motions for each site using the multiple stripes analysis method and convolved with the hazard estimates to produce site-dependent hazard curves, defining the mean annual frequency (MAF) of exceedance for the random variable of the maximum inter-storey drift ratio (MIDR). The performance of the DDBD method was assessed by evaluating the variability in the risk of the performance objective not being met, which indicated a performance range of approximately 1.0 – 1.8 times the MAF of the design intensity. It was found that, as a consequence of the dilution in response predictability caused by the power of uncertainties and the hazard characteristics in the vicinity of influential intensity levels, checking the probability of exceedance of the design intensity reveals little about the probability of exceedance of the target response. As a consequence, the present deterministic alternative of DDBD lacks the ability to bridge the gap between current structural design and the computationally demanding probabilistic methods embraced by pure PBEE.

Keywords: Direct Displacement-Based Design; Seismic Risk; Seismic Hazard; PBEE

ACKNOWLEDGEMENTS

TABLE OF CONTENTS

TABLE OF CONTENTS

LIST OF FIGURES

LIST OF TABLES

1 INTRODUCTION

In the early 1990s, Priestley [1993] identified many fundamental limitations in the current, code adopted force-based design philosophy, stimulating interest amongst researchers. As an attempt to mitigate the recognised deficiencies in traditional force-based design, a number of displacement-based design (DBD) procedures were developed and tested during the following decades [e.g. Sullivan *et al*., 2003]. One method that emerged during this process was the innovative design philosophy known as Direct Displacement-Based Design (DDBD) which is currently the most developed DBD method with a recent update to the subject text [Priestley *et al*., 2017] and includes a model code [Sullivan *et al*., 2012].

The fundamental philosophy behind the DDBD approach is to design buildings and bridges by proportioning strength and stiffness to achieve a given performance limit state under a specified level of seismic intensity. This is in contrast to traditional force-based design, where the satisfaction of the performance objective is checked at the end of the design process. It is often believed that, as the DDBD method designs directly to attain a given performance limit state, the resulting structures will have "essentially uniform-risk" of the performance objective not being met, and hence philosophically compatible with the seismic spectra incorporated in design codes that are assumed to have uniform-risk of being exceeded. Therefore, it can be interpreted that DDBD is akin to Performance-Based Earthquake Engineering methods [PBEE: Deierlein *et al*. 2003] or, at the very least, DDBD can be used as a deterministic tool to simplify the computationally expensive methods employed in Performance-Based Seismic Design (PBSD). This belief inherently relies on the assumption that deterministically checking the probability of exceedance at the design intensity level is equivalent to checking the probability of exceedance at the response level. Such a belief trusts, rather naively, that a simplified pseud-static method that is incapable of dealing with the complexities of the building's dynamic behaviour under the excitation of real ground motions is unaffected by uncertainties in ground motion characteristics at a given intensity level and uncertainties in the structural capacity. This reasoning requires quite a large leap of faith.

However, by acknowledging the uncertainty associated with the random variables defining the response capacity and the ground motion characteristics not only at the design level but at all influential ground motion intensities, the dispersion in the relationship linking the ground motion intensity to structural response can be estimated. When this relationship is combined with site-specific hazard estimates, the risk of exceeding any arbitrary limit state, such as life safety or collapse, can be quantified. In fact, as shown by Cornell *et al*. [2002], when considering the effects of both epistemic and aleatory sources of uncertainty, ground motion

levels less than the design intensity, which by definition occur more frequently, are also capable of contributing to the risk of violating the performance objective. Consequently, one must integrate across all scenarios that contribute to the mean annual frequency (MAF) of exceeding the performance objective using Equation 1.1.

$$\lambda(EDP > edp) = \int_0^{+\infty} P(EDP > edp | IM = x) \cdot |d\lambda_{IM}(x)| \qquad (1.1)$$

By employing a closed-form solution [Cornell *et al.*, 2002] to approximate Equation 1.1, given by Equation 1.2, Vamvatsikos *et al.* [2016] demonstrate the effects of uncertainties on the limit state performance with a simple example.

$$\lambda(EDP > edp) \approx P_o \cdot \exp\left(\frac{1}{2}k^2\beta_{T\theta}^2\right) \qquad (1.2)$$

Where P_o is the mean annual frequency of the design intensity, k is the hazard curve slope in log space at the design intensity, and $\beta_{T\theta}$ is the total dispersion in the IM-EDP relationship. For an ultimate limit state performance objective, typical values of k are between 2-4 and $\beta_{T\theta} \approx 0.4$. Therefore, for this simple example, it can be seen that the code-based design would have a MAF of approximately 1.4 – 3.6 times the MAF of the design intensity, and one is left to rely on other effects such as material overstrength to mitigate this amplification. Clearly, as a consequence of neglecting hazard characteristics other than that at the design ground motion intensity and the intrinsic uncertainty in the IM – EDP relationship, the degree of confidence in achieving the performance objective should be questioned.

The effects mentioned above, which dilute the predictability of the response, motivate the scope of this thesis to provide insight into the capabilities of DDBD in approaching the more robust response estimates that can be obtained with the advanced PBSD methods. Due to the highly complex relationship dictated by the structural system that maps the ground motion input to response output, the scope of the problem is limited to a single building so that variations in the response performance can be attributed to differences in the hazard characteristics. To accomplish this goal, a simple case study building is designed to achieve a single performance objective by applying the current Eurocode provisions and substituting DDBD for the code adopted equivalent lateral force method. Using the design spectrum recommended by EN1998 as the criteria, three high seismicity sites spread across Europe are identified as equally suitable locations for the case study building. For each site, the maximum inter-storey drift ratio (MIDR) hazard curve is computed using the Pacific Earthquake Engineering Research Center (PEER) PBEE methodology, initially outlined by Cornell and Krawinkler [2000].

The building performance is quantified by evaluating the site-specific MIDR hazard curves at the limit state capacity targeted by the DDBD method to quantify the variation in the mean annual frequency of the performance objective not being met at the three sites. The performance assessment is then extended to an objective not explicitly considered in the building design by quantifying the variation in the mean annual frequency of collapse.

2 CASE STUDY BUILDING

The Direct Displacement-Based Design method [DDBD: Priestley *et al.*, 2017] was used to produce a case study building suitable for three high seismicity sites across Europe. The building can be described as a four-storey ordinary office building (importance class II), 5-bays long by 3-bays wide. With an inter-storey height of 4.0 m and a consistent bay length of 8.0 m in both directions, the building stands at 16 m high with a plan geometry of 24 m by 40 m. The building layout is both regular in plan and elevation, and any 3D effects due to accidental eccentricity have been ignored for simplicity so that the building can be idealised as a simple 2D model for both design and analysis. The lateral load resisting system is provided by two pairs of identical reinforced concrete cantilever walls in the transverse direction and steel moment frames in the longitudinal direction. It is assumed that the distance between the two walls at each end of the building is large enough such that slab-coupling effects are negligible. The lateral load resisting system shown in blue by Figure 2.1a is assumed to have a fixed base, while the intermediate structure and gravity frames, shown in grey, utilise pinned connections such that they do not contribute significantly to the lateral resistance of the building. Furthermore, the analysis is limited to the transverse system only, with the longitudinal direction presented for completeness.

(a)

(b)   (c)
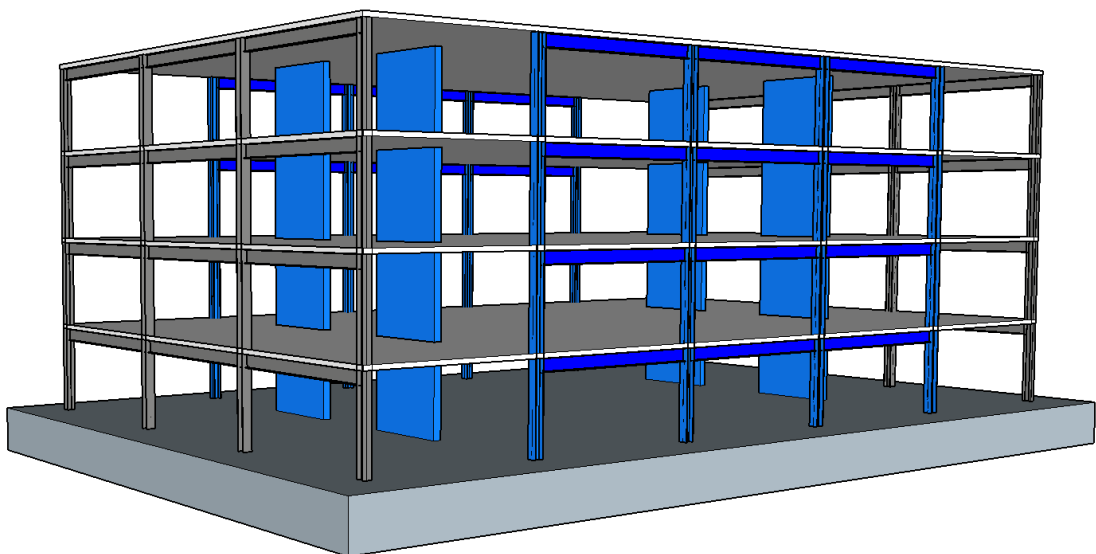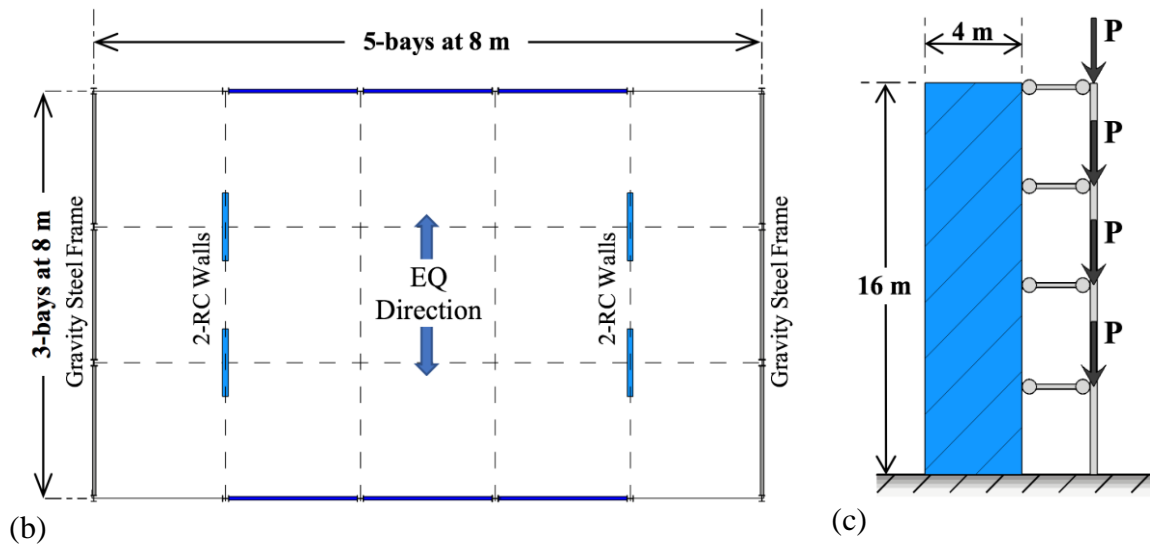
Figure 2.1 (a) Case study building (b) Building plan (c) Structural model

2.1   Direct Displacement Based Design

The building described above has been designed to satisfy the Life Safety limit state by imposing a drift limit of 2.0% at a design intensity with a 10% probability of exceedance (PoE) in 50 years; or equivalently, for an intensity with a return period of 475 years. It is assumed that the building contains non-structural elements fixed in such a way that they do not interfere with the structural deformations. Therefore, according to the current EN1998 standards, the drift limit of 2.0% at the design intensity is equivalent to the 1.0% drift limit of the damage limitation criteria at an intensity with a 10% probability of exceedance in 10 years. The Life Safety (LS) limit state is the only performance objective employed in the design procedure.

Following the approach by Kohrangi *et al.* [2017], three high seismicity sites in Athens, Perugia and Focsani were selected to anchor the case study building as they share a common reference peak ground acceleration (PGA) of $a_g = 0.3g$ at the design intensity level with 10% PoE in 50 years [EFEHR, 2017]. The Type 1 design spectrum recommended by EN1998 for high-seismicity regions is rigidly anchored to this common reference PGA value. Therefore, provided the soil class is consistent for all sites, the resulting design spectrum is identical, and hence the building is equally suitable for any of the three locations considered. The specific site coordinates and geographical locations are shown in Table 2.1 and Figure 2.2, respectively.

Table 2.1 Case study building coordinates

	Athens	Perugia	Focsani
Latitude	37.976	43.111	45.696
Longitude	23.751	12.389	27.179

Figure 2.2 Selected building sites

For the purpose of design and analysis, it is assumed that all three sites have a soil profile that produces a shear wave velocity in the top 30 m of $V_{s30} = 360$ ms^{-1} (borderline of Soil Type C). The Type 1 elastic response spectrum shown in Figure 2.3 is therefore defined by the periods of $T_B = 0.2$ s, $T_C = 0.6$ s, and $T_D = 2.0$ s and with a soil amplification factor of $S = 1.15$. It is also assumed that the peak displacement response is governed by the equations of steady-state sinusoidal response. Hence, the design spectral displacement for 5% equivalent viscous damping can be generated from the acceleration spectrum with the following relationship.

$$S_d(T) = \frac{T^2}{4\pi^2} S_a(T) \cdot g \tag{2.1}$$

Where g is the acceleration due to gravity and $S_a(T)$ is expressed as a multiple of g. In recognition of the fact that the corner period is a function of the earthquake magnitude and that the cut-off corner period of 2.0 s given by EN1998 is non-conservative in computing the displacement response spectra [Priestley *et al.*, 2017; Faccioli *et al.*, 2004], the constant velocity region of the response spectrum is continued into the constant displacement region until the corner period shown in Figure 2.3. Beyond this period, the spectral displacement is assumed to remain constant.
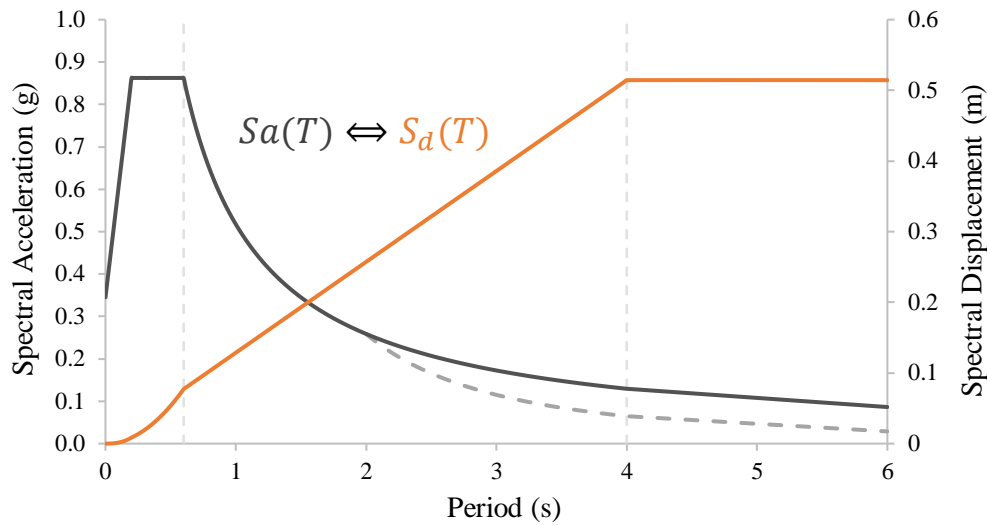
Figure 2.3 Design spectral acceleration and displacement

The corner period of 4.0 s shown in Figure 2.3 is estimated with the relationship proposed by Faccioli *et al.* given by Equation 2.2, assuming that the hazard is dominated by a magnitude $M_w = 6.9$ at the level of seismicity considered.

$$T_c = 1.0 + 2.5(M_w - 5.7) \tag{2.2}$$

It is assumed that the occupancies of the four storeys are correlated, and a reduced live load of $Q_E = 1.0$ kPa is imposed on every level except the roof. The dead weights, G, for each floor have been estimated with allowances of 2.4 kPa and 4.9 kPa for the gravity structure and a 200 mm thick reinforced concrete slab, respectively. An additional allowance of 1.0 kPa for external cladding, equivalent to 0.3 kPa/floor area, and 0.5 kPa for finishes have also been made. Furthermore, a superimposed dead load of 3.1 kPa has been assumed at roof level allowing for lightweight plant equipment and 1.7 kPa at all other levels for non-structural elements and services. With the aggregated weights shown in Table 2.2 and a total loaded floor area of 982 m² at each level, the total seismic weight of the building was estimated to be 42400 kN.

Table 2.2 Aggregated building weights

Level	Seismic live load (kPa)	Dead loads (kPa)		Seismic weight		Seismic mass
		SDL	G	(kPa)	(kN)	(T)
Roof	0.0	3.1	7.7	10.81	10620	1082
Level 1	1.0	1.7	8.1	10.79	10590	1080
Level 2	1.0	1.7	8.1	10.79	10590	1080
Level 3	1.0	1.7	8.1	10.79	10590	1080

The material properties considered are, for concrete, a characteristic strength of $f'_c = 30$ MPa and elastic modulus of 29 GPa and for all reinforcement, Grade 75 reinforcing steel with characteristic strength of $f_y = 500$ MPa with an elastic modulus of 200 GPa. The effective material properties are used to design the intended plastic hinge locations as given by Equations

2.3a and 2.3b, and flexural strength reduction factors will not be used due to the issues discussed in [Priestley *et al.*, 2017]. However, in the design of the transverse reinforcement to provide adequate shear strength, material strength reduction factors are used in accordance with the Eurocode provisions.

$$\text{Concrete:} \quad f'_{ce} = 1.3f'_c \tag{2.3a}$$

$$\text{Steel:} \quad f_{ye} = 1.1f_y \tag{2.3b}$$

Due to the regular building configuration, the seismic mass per floor is equally divided between the two pairs of identical structural walls, with a length of 4.0 m and thickness of 0.30 m, at each end of the building.

Unlike traditional force-based design, which characterises the structure in terms of the elastic, pre-yield properties, DDBD characterises the structure by its secant stiffness K_e at the maximum displacement Δ_d as shown in Figure 2.4. In lieu of the arbitrary ductility allocation in the form of a force reduction factor assigned to the system as a whole and without consideration of displacement compatibility, DDBD accounts for energy dissipation with the assignment of equivalent viscous damping ξ, at a level representative of the combined elastic damping and the hysteretic energy absorbed during inelastic response. However, for essentially all real buildings with multiple degrees of freedom, the method relies on the substitute structure approach [Shibata and Sozen, 1976], in which the equivalent mass m_e, design displacement Δ_d, and the effective damping ξ_e are determined in terms of an equivalent single-degree of freedom system. Once the characteristics of the substitute structure are determined, the design base shear is calculated and distributed to discretised mass locations up the height of the real building in proportion to the mass and design inelastic displacement, similar to force-based design.
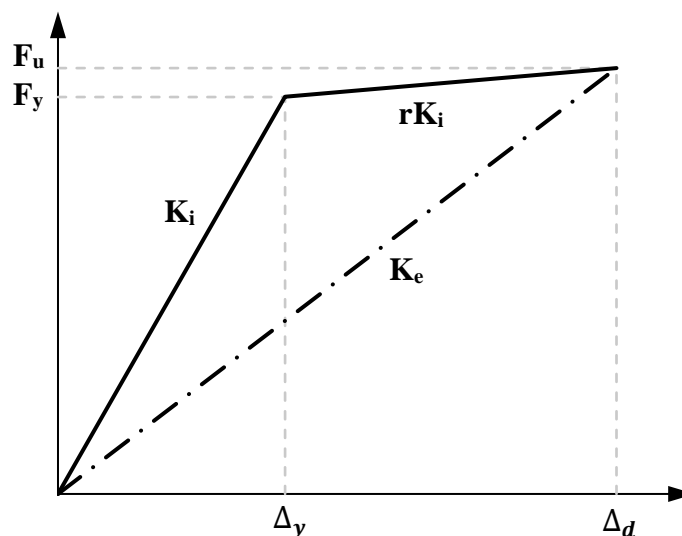

Figure 2.4 DDBD approach

The design displacement of the substitute structure is calculated with Equation 2.4 by assuming an inelastic displaced shape of the first mode response given by Equation 2.5, which is consistent with the structure's characterisation using the secant stiffness at the maximum response.

$$\Delta_d = \sum_{i=1}^{n}(m_i \Delta_i^2) / \sum_{i=1}^{n}(m_i \Delta_i) \tag{2.4}$$

Where m_i and Δ_i are the masses and displacements at the n discretised locations. In this case, the mass is discretised at the four-floor levels and $m_i = m$ as the seismic mass is consistent at all levels.

$$\Delta_i = \Delta_{yi} + \Delta_{pi} \tag{2.5}$$

For the cantilever wall building of interest, the governing inter-storey drift will occur in the top storey. Assuming that at yield, the first mode curvature distribution is triangular with height and that all plastic rotation is concentrated at the base of the wall, the two terms of Equation 2.5 can be calculated with Equations 2.6a and 2.6b and the governing inter-storey drift, θ_{dn}, is calculated using Equation 2.7.

$$\Delta_{yi} = \frac{\varepsilon_y}{l_w} H_i^2 \left(1 - \frac{H_i}{3H_n}\right) \tag{2.6a}$$

$$\Delta_{pi} = \theta_{pn} H_i \tag{2.6b}$$

$$\theta_{dn} = \theta_{yn} + \theta_{pn} \tag{2.7}$$

Where θ_{yn} is the yield rotation given by Equation 2.8a. θ_{pn}, given by Equation 2.8b, is the allowable plastic rotation that can develop at the base of the wall while simultaneously satisfying the limit state drift of 2.0% and the damage control curvature limits ϕ_{dc}. Where, ϕ_{dc} has been derived with limiting material strains of $\varepsilon_s = 0.06$ for steel and $\varepsilon_c = 0.018$ for confined concrete.

$$\theta_{yn} = \frac{\phi_y H_n}{2} \tag{2.8a}$$

$$\theta_{pn} = min\{\theta_{dn} - \theta_{yn}, (\phi_{dc} - \phi_y)L_p\} \tag{2.8b}$$

Where the yield curvature can be estimated with the relationship, $\phi_y = 2\varepsilon_y/l_w$, and the damage control curvature limit can be adequately approximated by, $\phi_{dc} = 0.072/l_w$ for rectangular walls with uniformly distributed reinforcement. Lastly, L_p is the plastic hinge length over which the plastic curvature is considered constant and is calculated using Equation 2.9a.

$$L_p = kH_e + 0.1L_w + L_{sp} \tag{2.9a}$$

$$k = 0.2\left(\frac{f_u}{f_y} - 1\right) \leq 0.08 \tag{2.9b}$$

$$L_{sp} = 0.022f_{ye}d_{bl} \tag{2.9c}$$

Therefore, the yield rotation of the 4 m long, 16 m high structural wall is:

$$\theta_{yn} = \left(\frac{2}{4_m} \cdot \frac{550_{MPa}}{200_{GPa}}\right)\frac{16_m}{2} = 1.1\%$$

And with the allowable curvature limit satisfying material strains, of:

$$\phi_{dc} = \frac{0.072}{4_m} = 0.018 \ m^{-1}$$

Giving an allowable plastic rotation of:

$\theta_{pn} = min\{2.0\% - 1.1\%, (0.018 - 0.00138)1.45_m\}$
$\theta_{pn} = min\{0.9\%, 2.4\%\}$
$\theta_{pn} = 0.9\% \Longrightarrow$ code drift of 2.0% governs the design

The plastic hinge length has been calculated assuming f_u/f_y=1.3, d_{bl} = 25 mm and H_e= 12.4 m. Although the effective height of the wall is unknown at this stage of design, it is reasonable to substitute the wall height for H_e in the calculation of the plastic hinge length. However, in cases with a low margin between the code drift governing, a more accurate estimation of the plastic hinge length may be required. In this case, assuming the effective height is equal to the wall height results in an overestimation of the plastic hinge length of only 0.22 m.

The displacement profile at yield, Δ_{yi}, can be determined with Equation 2.6a. With the substitution of the above result into Equation 2.6b, the additional plastic displacement, Δ_{pi}, can be added to give the design displacement profile and the corresponding inter-storey drift ratio (IDR) as shown in Figure 2.5. The results of the intermediate calculations are shown in Table 2.3.
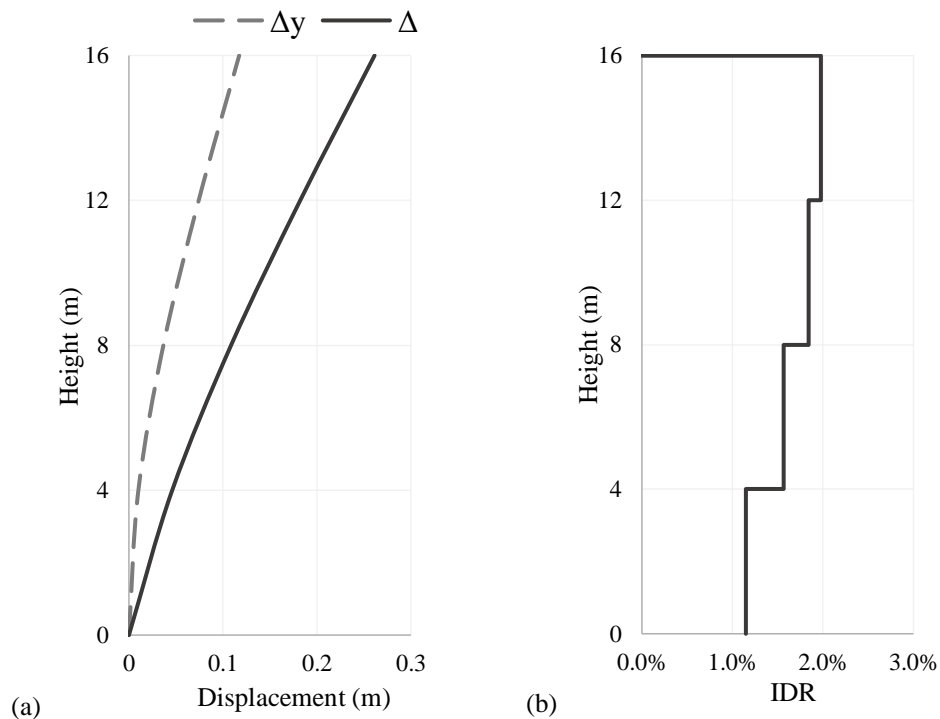
Figure 2.5 Design drift profile (a) and corresponding design IDR (b)

Table 2.3 Intermediate calculation results

Level	H_i	Δ_{yi}	Δ_i	m_i	$m_i\Delta_i$	$m_i\Delta_i^2$	$m_i\Delta_iH_i$	IDR
4	16	0.12	0.26	540	141	36.9	2260	2.0%
3	12	0.07	0.18	540	98	17.9	1180	1.8%
2	8	0.04	0.11	540	59	6.4	469	1.6%
1	4	0.01	0.05	540	25	1.1	100	1.2%
			$\sum =$	**2160**	**323**	**62.3**	**4008**	

Where all dimensions are given in metres and mass in tonnes

As per Equation 2.4, the design displacement of the substitute structure, Δ_d, is calculated by taking the ratio of the sums of columns 6 and 7 of Table 2.3.

$\Delta_d = 62.3/323$
$\Delta_d = 0.19\ m$

The effective mass and height of the substitute structure are calculated using Equations 2.10 and 2.11.

$$m_e = \frac{1}{\Delta_d}\sum_{i=1}^{n}(m_i\,\Delta_i) \tag{2.10}$$

$m_e = \frac{1}{0.19}(323) = 1675\ tonnes$ (78% of the total seismic mass)

And,

$$H_e = \sum_{i=1}^{n}(m_i\,\Delta_iH_i)\,/\sum_{i=1}^{n}(m_i\,\Delta_i) \tag{2.11}$$

$H_e = 4008/323$
$H_e = 12.4\ m$

By substituting $H_i = H_e$ into Equation 2.6a the yield displacement of the substitute structure is calculated to be:

$$\Delta_y = \frac{\varepsilon_y}{l_w}H_e^2\left(1 - \frac{H_e}{3H_n}\right)$$

$$\Delta_y = \frac{0.00275}{4}12.4^2\left(1 - \frac{12.4}{3 \times 16}\right)$$

$\Delta_y = 0.078\ m$

Which gives a system ductility demand at a design displacement that is compatible with the limiting drift of 2.0% calculated with Equation 2.12:

$$\mu = \frac{\Delta_d}{\Delta_y} \tag{2.12}$$

$$\mu = \frac{0.19}{0.078}$$

$\mu = 2.46$

The design equivalent viscous damping ratio for 5% elastic damping is estimated with Equation 2.13 using the Takeda Thin hysteretic relationship to represent the response of the ductile reinforced concrete wall structure.

$$\xi_e = 0.05 + 0.444\left(\frac{\mu - 1}{\mu\pi}\right) \tag{2.13}$$

$$\xi_e = 0.05 + 0.444\left(\frac{1.44}{2.46\pi}\right) = 13.4\%$$

Assuming normal conditions apply (i.e. velocity pulse type ground motions are not considered), the inelastic displacement response spectra shown in Figure 2.6, which is consistent with 13% equivalent viscous damping, is computed by applying the modification factor R_ξ to the elastic design spectrum given in Figure 2.3.

$$R_\xi = \left(\frac{0.07}{0.02 + \xi_e}\right)^{0.5} \geq 0.55 \tag{2.14}$$

$$R_\xi = \left(\frac{0.07}{0.02 + 0.133}\right)^{0.5} = 0.67$$
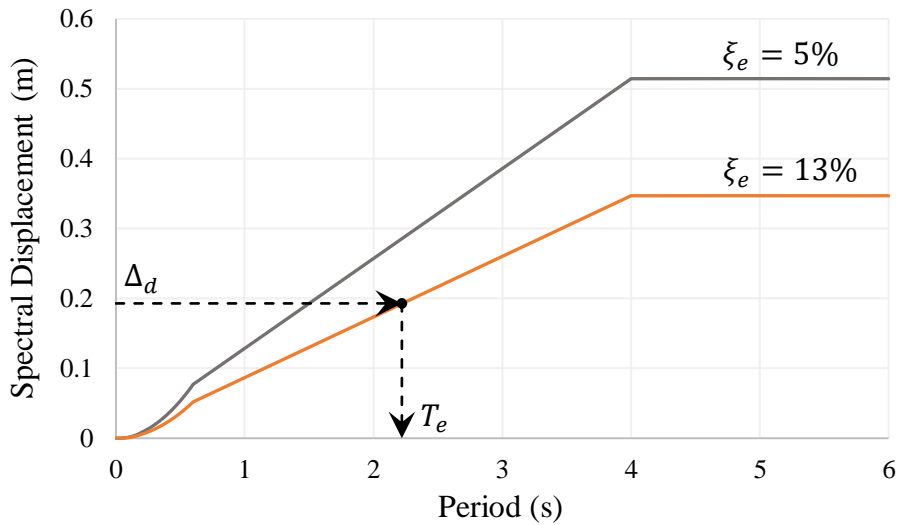
Figure 2.6 Design displacement spectrum

Thus, the effective period T_e, of the substitute structure at the maximum displacement response Δ_d, can be read directly from the inelastic displacement spectra as $T_e = 2.2s$. By inverting the equation for the period of an SDOF oscillator (Equation 2.15) and substituting for the effective period and mass calculated previously, the effective stiffness, K_e, of the substitute structure is determined to be:

$$K_e = \frac{4\pi^2 m_e}{T_e^2} \tag{2.15}$$

$$K_e = \frac{4\pi^2(1675)}{2.22^2} = 13414 \ kNm^{-1}$$

Applying Hooke's law, the design base shear is thus given by Equation 2.16

$$V_{base} = K_e\Delta_d \qquad (2.16)$$

$$V_{base} = 13414 \ kNm^{-1} \times 0.19 \ m$$

$$V_{base} = 2588 \ kN$$

Although P-Δ effects are not considered to be significant for this structure, the required strength has been enhanced to account for the additional demand acting on the walls as the structure displaces to the design displacement. Therefore, the total required strength has been provided in accordance with Equation 2.17, where the coefficient, C = 0.5 for concrete structures in recognition of the additional energy dissipation and the low stability index of this structure.

$$V_{base} = K_e\Delta_d + C \cdot P\Delta_d/H_e \qquad (2.17)$$

$$V_{base} = 2588 + 0.5(2160 \times 9.81)kN\left(\frac{0.19}{12.4}\right)$$

$$V_{base} = 2750 \ kN$$

The base shear is then distributed between the discretised mass locations of the MDOF system as design forces in proportion to the mass and design inelastic displacement as determined by Equation 2.18.

$$F_i = V_{base}(m_i\Delta_i) / \sum_{i=1}^{n}(m_i \Delta_i) \qquad (2.18)$$

Figure 2.7 Design lateral forces

Having now established the distribution of equivalent lateral design forces acting up the height of the real building as shown in Figure 2.7, the design moments of the potential plastic hinges can be determined. Further determination of the required distributi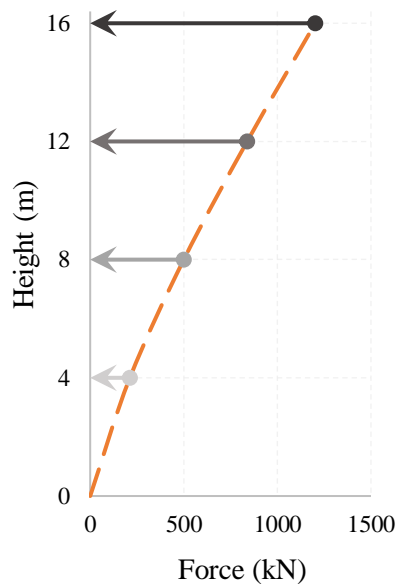on of flexural and shear strength up the height of the cantilever walls, accounting for the flexural overstrength capacity, $\phi^o M_B$, at the wall-base is established using the simplified capacity design approach such that non-ductile modes of inelastic deformations are prevented. The walls are detailed to satisfy these demands in accordance with the EN1998 dDuctility Class High (DCH) provisions.

The bi-linear capacity-design moment envelope is defined by the overstrength base moment capacity, $\phi^o M_B$, the mid-height overstrength moment $M_{0.5H}^o$ (Equation 2.19), and zero moment at the top of the wall. Figure 2.8a compares the moment capacity provided by the reinforcement configurations shown in Table 2.4 to the capacity-design demand. A conservative tension shift dimension of half the wall length has been considered in the curtailment of flexural reinforcement. The flexural overstrength factor, ϕ^o, used in Equation 2.19 is taken as 1.0 as the effect of strain hardening has been accounted for in the DDBD process for determining the required flexural reinforcement at the base of the wall (i.e. Equation 2.3).

$$M_{0.5H}^o = C_{1,T} \cdot \phi^o M_B \quad \text{where,} \quad C_{1,T} = 0.4 + 0.075 T_i \left(\frac{\mu}{\phi^o} - 1 \right) \geq 0.4 \tag{2.19}$$

With the initial elastic period, T_i, estimated using Equation 2.20, assuming a post-yield stiffness of 5%.

$$T_i = T_e \sqrt{\frac{1 + 0.05(\mu_{sys} - 1)}{\mu_{sys}}} \tag{2.20}$$

$T_i = 1.47$ seconds

Hence,

$$M_{0.5H}^o = 0.56 \phi^o M_B$$

The overstrength shear force demand envelope shown in Figure 2.8b is defined by a straight line, anchored at an overstrength shear demand of V_{base}^o defined by Equation 2.21a, at the base of the wall to a minimum demand of V_n^o defined by Equation 2.21b, at the top of the wall. For the purpose of this preliminary design, the overstrength factor, ϕ^o, used in the determination of the shear demand has been conservatively taken as the default value of 1.25. However, as shown by the pushover analysis in Section 2.3, the overstrength moment capacity achieved shows that further refinement is possible if required.

$$V_{base}^o = \phi^o \omega_V V_{base} \quad \text{with,} \quad \omega_V = 1 + \frac{\mu}{\phi^o} C_{2,T} \tag{2.21a}$$

$$V_n^o = C_{3,T} V_{base}^o \tag{2.21b}$$

Where the coefficients $C_{2,T}$ and $C_{3,T}$ are given by Equations 2.22a and 2.22b

$$C_{2,T} = 0.067 + 0.4(T_i - 0.5) \leq 1.15 \tag{2.22a}$$
$$C_{2,T} = 0.45$$
$$C_{3,T} = 0.9 - 0.3 T_i \geq 0.3 \tag{2.22b}$$
$$C_{3,T} = 0.46$$

The transverse shear reinforcement shown in Table 2.4 has been provided such that the overstrength demand, defined by the following parameters, is exceeded up the height of the building.

$$V_{base}^o = 1.25 \left(1 + \frac{2.46}{1.25} 0.46\right) 1375 \; kN$$

$$V_{base}^o = 3256 \; kN \; (per \; wall)$$

$$V_n^o = 0.46 \times 3256 \; kN$$

$$V_n^o = 1498 \; kN$$
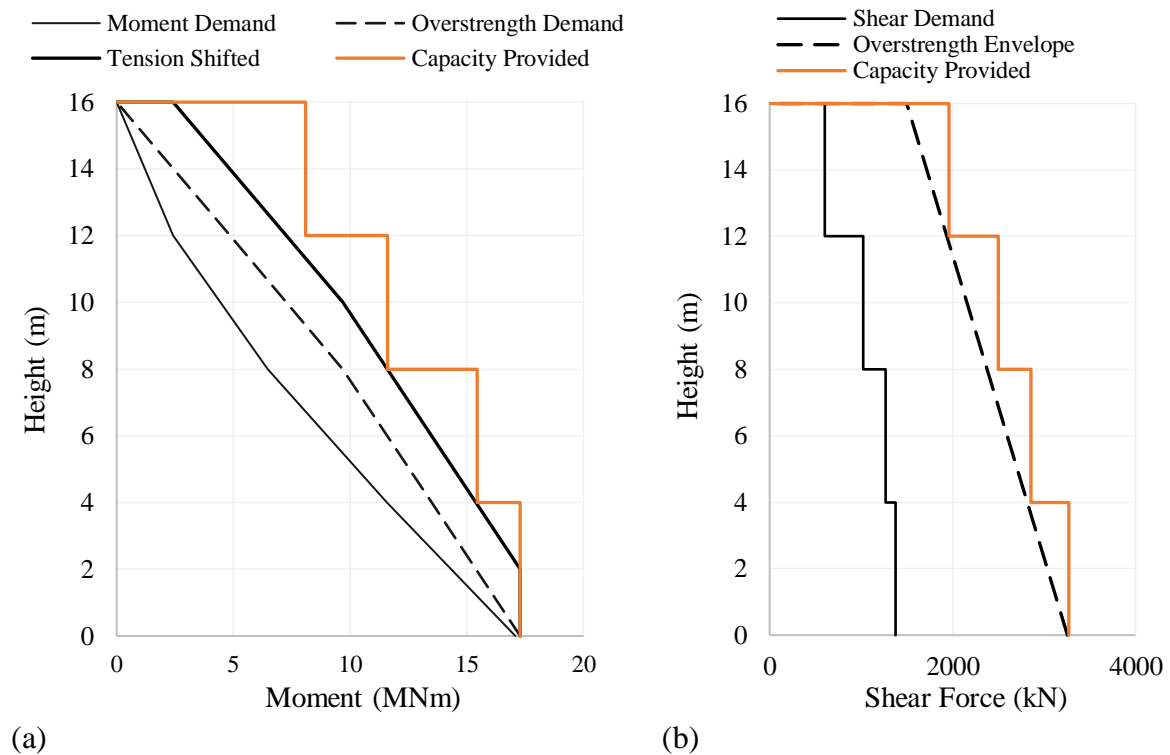
Figure 2.8 Capacity envelope for (a) design moment and (b) design shear

Table 2.4 Provided section reinforcement

	Section	Longitudinal	ρ_t	Transverse
Level 1	BE	6-rows of 2-Ø20	1.16%	Ø14 @ 100crs vertically, restraining all longitudinal steel
	Web	16-rows of 2-Ø16		Ø12 @ 125crs vertically
Level 2	BE	6-rows of 2-Ø20	1.06%	Ø12 @ 125crs vertically, restraining all longitudinal steel
	Web	13-rows of 2-Ø16		Ø12 @ 150crs vertically
Level 3	BE	5-rows of 2-Ø16	0.80%	Ø12 @ 150crs vertically, restraining all longitudinal steel
	Web	14-rows of 2-Ø16		Ø12 @ 150crs vertically
Level 4	–	17-rows of 2-Ø16 Uniformly spaced	0.57%	Ø12 @ 150crs restraining all longitudinal compression steel

2.2   Structural Modelling

Producing reliable estimates of the building's maximum inter-storey drift ratio (MIDR) hazard requires a model that can accurately predict the structural response for a spectrum of ground motion intensity levels. Low-intensity levels contribute the most to damage and economic loss as they produce low levels of inter-storey drift that occur frequently. Whereas, high-intensity levels that occur less frequently contribute the most to the collapse risk as they are capable of causing large levels of inter-storey drift. However, it can be difficult to produce a structural model capable of accurately representing the dynamic behaviour over this wide range of intensity levels. The model should be capable of capturing the effects of concrete cracking and tension stiffening that are important at low displacements while still accurately predicting strength and stiffness deterioration at large displacements [Goulet *et al*., 2007]. As discussed by Deierlein [2003], in order to accurately predict the structural response at displacements that lead to structural collapse, it is essential that the dynamic model incorporates strength deterioration (deformation-softening) in addition to stiffness deterioration (stiffness-softening) caused by the cyclic response induced by the ground motion.

One option is to use a lumped plasticity model with the hysteretic parameters calibrated using experimental results of reinforced concrete component tests that incorporates both strength and stiffness deterioration [Zareian and Krawinkler, 2007]. However, the alternative of a fibre-based element model will be adopted in this study as both stiffness and strength deterioration due to concrete cracking, section yielding, and cyclic loading are inherent in the model. The building has been modelled using SeismoStruct [SeismoStruct, 2018] with inelastic displacement-based frame elements capable of fully accounting for the distribution of material inelasticity up the wall height and throughout the cross-sectional depth. The constitutive material models adopted to define the nonlinear behaviour of the reinforced concrete walls with the characteristic strengths defined above, are; for concrete, the Mander *et al.* model [1988], and for the reinforcement, Menegotto-Pinto steel model. The Mander *et al.* model has incorporated the confinement effects of the transverse reinforcement shown in Table 2.4 and assumes that the confining stress provided by the stirrups is maintained throughout the structural response. The Menegotto-Pinto steel model has been calibrated assuming 5% strain hardening with a tensile fracture defined by a limiting strain of 10%. Furthermore, a notification flag has been included in the model to indicate buckling of longitudinal reinforcement at a strain equal to the ultimate crushing strain of the confined concrete core.

Consistent with the design assumption, the seismic mass has been lumped at the four floor levels, and the floor diaphragms are assumed to be infinitely stiff in-plane while flexible out-of-plane. The floor diaphragms are assumed to be capable of distributing the inertial forces evenly between the four identical structural walls, and therefore the model of the regular building was simplified by modelling the response of a single wall. As indicated in Figure 2.1c, the P-Δ effects of the gravity structure have been accounted for by allocating the tributary gravity load of each level to a fictitious leaning column element that is translationally slaved to the corresponding diaphragm level.

The model assumes a relatively low level of inherent damping as hysteretic energy dissipation is implicitly included within the nonlinear fibre element model formulation. The initial stiffness Rayleigh damping model has been adopted, assuming an equivalent viscous damping

coefficient of 1% anchored at the first and second modal periods of the structure. Furthermore, it is assumed that the effects of soil-structure interaction (SSI) will have an insignificant influence on the conclusions of this study and have therefore not been considered by the structural model.

2.3   Preliminary Structural Assessment

A preliminary structural assessment was performed to determine the structural characteristics required to inform the dynamic analysis and to verify the building's base shear capacity. An eigenvalue analysis was performed to produce the modal properties of the first three modes as shown in Figure 2.9.

Mode 1
$T_1 = 0.66s$
$m_e = 70\%$

Mode 2
$T_2 = 0.10s$
$m_e = 21\%$

Mode 3
$T_3 = 0.04s$
$m_e = 7\%$
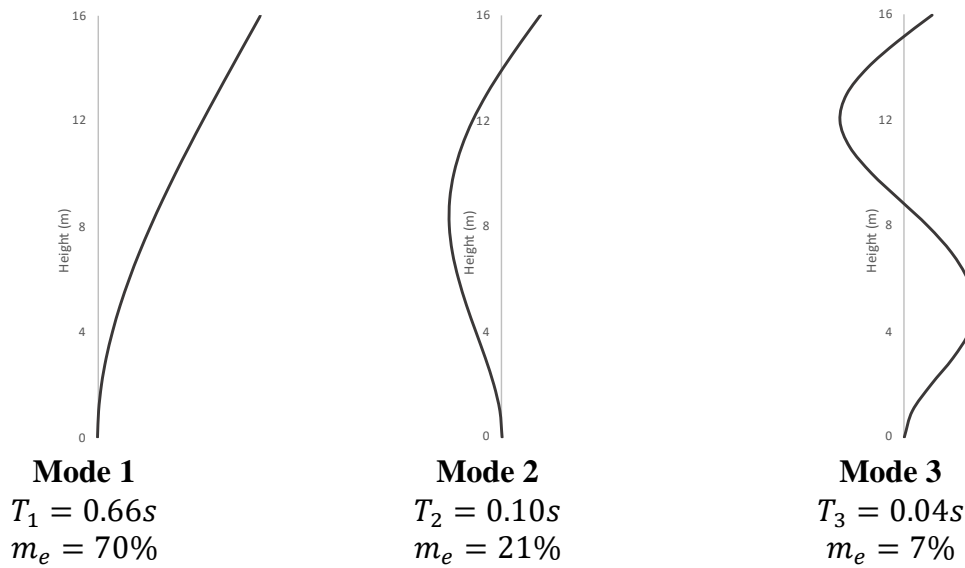
Figure 2.9 Eigen value analysis results

To verify the base shear capacity of the building design, a pushover analysis was performed with an imposed load pattern consistent with the assumed inelastic first mode shape adopted by the DDBD procedure. The pushover response was fitted with an idealised bi-linear curve with a yield displacement defined by the intersection of the line through the origin with secant stiffness through first yield and the nominal strength as shown in Figure 2.10. The resulting yield displacement is Δ_y= 0.084 m with a corresponding effective period estimated using Equation 2.23.

$$T_{eff} = T_{ela} \sqrt{\frac{k_{ela}}{k_{eff}}} \tag{2.23}$$

$$T_{eff} = 0.66 \sqrt{\frac{61810}{15435}}$$

$$T_{eff} = 1.32 \ s$$
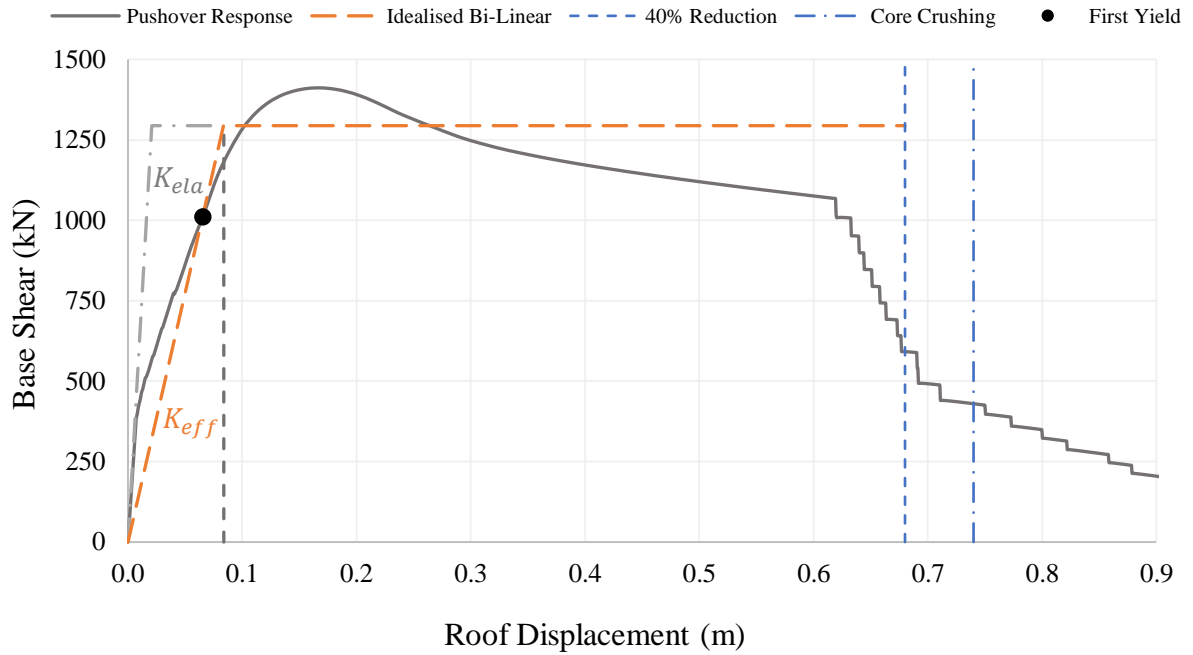
Figure 2.10 Pushover response

2.4 Collapse Capacity Estimation

The collapse capacity of the case study building has been estimated assuming that vertical failure modes, such as axial instability or shear failure, will be preceded by a side-sway collapse mechanism. Structural collapse has been said to occur if either the dynamic analysis algorithm fails to converge due to numerical instability at high deformation levels or if the maximum inter-storey drift ratio (MIDR) exceeds a limiting threshold value, θ_{col}, that causes the validity of the structural model to become questionable. It is likely that estimated collapse capacity is somewhat conservative; however, it is assumed that collapse will occur shortly after θ_{col} is exceeded.

The collapse capacity has been estimated from the pushover analysis shown in Figure 2.10 and has been taken as the minimum MIDR corresponding to either a sudden reduction of 40% in the building strength or the point corresponding to the concrete core crushing and buckling of flexural reinforcement. As shown in Figure 2.10, the former criterion governs the collapse capacity and corresponds to a MIDR of 4.5% and a global collapse ductility capacity of approximately $\mu_{\Delta,col} = 8$.

3 CONNECTING HAZARD TO STRUCTURAL RESPONSE

3.1 The Link Between Engineering Seismology and Earthquake Engineering

To facilitate the computation of the mean annual frequency of exceeding the limit state drift threshold ($\mathrm{MAF_{LS}} = \lambda(EDP > edp)$), a connection must first be made between the hazard at the site (engineering seismology) and the structural response (earthquake engineering). The robustness of this link is affected by the many simplifying assumptions of reality which can be detrimental to the accuracy of the estimated $\mathrm{MAF_{LS}}$. This chapter identifies three aspects that influence the robustness of this link and attempts to find a suitable balance between simplicity and accuracy of each component that, when combined, renders a reliable estimate of the $\mathrm{MAF_{LS}}$.

The $\mathrm{MAF_{LS}}$ can be calculated using Equation 3.1, by convolving, for all seismic sources, the probability of exceeding the limit state drift threshold, given the occurrence of an earthquake scenario, with the probability of such a scenario occurring.

$$\lambda(EDP > edp) = \sum_{i=1}^{n} \lambda_{0,i} \iiint P(EDP > edp | im, \mathrm{m}, \mathrm{r}) \cdot f_{\mathrm{IM}|M_i,R_i}(im|m,r) \cdot f_{M_i,R_i}(m,r) \, dr \, dm \, d(im) \quad (3.1)$$

Where $\lambda_{0,i}$ is the mean annual rate of occurrence of an event with a magnitude greater than m_{min} for source i, of n influential seismic sources. The probability of the engineering demand parameter EDP exceeding the limit state capacity edp, given the occurrence of an event scenario with magnitude m, distance r, producing a ground motion at the site with intensity level im, is given by the probability valued function $P(EDP > edp | im, \mathrm{m}, \mathrm{r})$. The probability of exceeding the intensity level im, given the event scenario, is characterised by the probability density function $f_{IM|M_i,R_i}(im|m,r)$ and the probability of that particular combination of magnitude and distance occurring is described by $f_{M_i,R_i}(m,r)$. For simplicity, Equation 3.1 has implied that the response EDP is only affected by the ground motion intensity, earthquake magnitude and source to site distance; however, the response may also be dependent on many other ground motion characteristics not represented here.

The computational effort of Equation 3.1 can be significantly simplified if the conditioning intensity measure is deemed sufficient. That is, all relevant characteristics of the hazard influencing the distribution of the structural response are captured by the conditioning IM and therefore, $P(EDP > edp|IM = im, M = m, R = r) = P(EDP > edp|IM = im)$ which leads to the more common form of Equation 3.1 given by Equation 3.2

$$\lambda(EDP > edp) = \int_{0}^{+\infty} P(EDP > edp|IM = x) \cdot |d\lambda_{IM}(x)| \qquad (3.2)$$

Sufficiency of the IM chosen to condition the response is a powerful property as it decouples the probabilistic quantification of the structural response given by the fragility function, $P(EDP > edp|IM = x)$, from the seismic hazard $\lambda_{IM}(x)$. The fragility function is often estimated analytically by structural engineers, using the results of nonlinear dynamic analyses of the given structure for a suite of earthquake ground-motion records. And, probabilistic seismic hazard analysis [PSHA: Cornell, 1968], generally carried out by seismologists, is typically used for site-specific hazard assessment to quantify the annual rate of exceeding each ground motion intensity level, $IM = x$. However, due to the highly complex relationship between the ground motion characteristics and the structural response of a multi-degree-of-freedom system, it is unlikely that a single scalar IM can entirely describe the causal characteristics of the ground motion while still producing an accurate estimate of the EDP distribution. Consequently, in reality, this equality is only approximate for most structures, and thus, a degree of bias may be introduced in the distribution of the EDP.

It is evident from the form of Equation 3.2 that the accuracy of the MAF$_{LS}$ is highly dependent on the quality of the IM chosen to condition the response, but also the characteristics of the ground motion set selected for the computation of the fragility function and the efficiency of the method used to compute the fragility function itself. The degree of complexity of each component can vary considerably, but inaccuracies introduced by the simplification of one aspect can be somewhat recovered by the other two.

3.2 Intensity Measure Selection

The quality of an intensity measure in terms of its ability to accurately predict the MAF$_{LS}$, within the probabilistic structural assessment framework given by Equation 3.2, is often judged by its three attributes: efficiency, sufficiency and practicality [Luco and Cornell, 2007]. With regards to the prediction of the structural response, an intensity measure is said to be efficient if the response, conditioned on that IM, has low variability (i.e. smaller $\sigma_{EDP|IM}$). Efficiency is a desired property of the conditioning IM, as the more efficient the IM is, the fewer the number of required ground motion records needed to perform nonlinear response analysis to reach stable estimates of the EDP|IM relationship with the desired precision. Whereas, a sufficient intensity measure is one that is capable of fully describing all characteristics of the ground motion that influence the structural response. That is, the distribution of the response EDP, conditioned on the chosen IM, is independent of all other characteristics that may be present in the ground-motion set. Unfortunately, such an IM simply does not exist for realistic applications. As discussed by Luco and Cornell [2007], the calculation of the MAF$_{LS}$ is simply

an application of the total probability theorem, so theoretically, the MAF$_{LS}$ obtained with Equation 3.2 should be independent of the choice of IM. However, as mentioned in Section 3.1, the fragility function, given by $P(EDP > edp|IM = x)$, is often estimated analytically using the results of nonlinear dynamic analyses for a limited number of ground-motion records characterised by the IM. If the chosen intensity measure is not sufficient, the estimate of the MAF$_{LS}$ will be somewhat dependent on the set of ground motions used to estimate the structural response, and therefore the estimate of MAF$_{LS}$ will be biased. Hence, sufficiency is a desired property as it enables unbiased estimates to be obtained, regardless of the chosen ground motion set used to estimate the fragility function. However, an intensity measure that is both efficient and sufficient is of no use if no reliable means exist to compute the occurrence of different IM levels given the occurrence of any given event scenario. This leads to the attribute of practicality which refers to the ability to predict the occurrence of the IM such that $\lambda_{IM}(x)$ can be computed. The practicality of the IM relies on the existence of ground motion prediction models (GMPMs) that can predict the occurrence of the chosen IM within an acceptable degree of accuracy, i.e. the uncertainty in the IM itself given the occurrence of an earthquake rupture scenario, $\sigma_{IM|rup}$.

The intensity measure chosen to quantify the severity of the ground motion can be defined purely by the ground motion properties, such as the peak ground acceleration, or on both the ground motion and structural properties, such as spectral acceleration at or near the first mode period of the structure, Sa(T$_i$) [L. Eads, E. Miranda and D. Lignos, 2015]. Previous research has shown that choosing a quality intensity measure to link the hazard to the structural response is not a straightforward task [Kohrangi *et al.*, 2016; Luco and Cornell, 2007], and a range of legitimate IMs can give very different estimations for the distribution of the structural response. Although the true response distribution is unknown to the analyst, the properties of efficiency and sufficiency can be used to argue why a particular IM provides a better estimate of the MAF$_{LS}$.

Various studies have shown that the quality of the IM choice is somewhat unique to the particular problem of interest. This is due to the fact that the efficiency and sufficiency of the IM are dependent on the structure being considered, the response EDP of interest and the building site exposed to the seismic hazard. For example, the two EDPs of the inter-storey drift ratio (IDR) and the peak floor acceleration (PFA), both of which are highly correlated with damage, are best predicted by different scalar IMs [Kohrangi *et al.*, 2016]. Furthermore, the suitability of the selected IM for the accurate prediction of the IDR is a function of both the physical and dynamic characteristics of the building in addition to the degree of nonlinearity at which the response is being predicted. For example, spectral acceleration at an elongated period has been shown to be a relatively accurate predictor of IDR in the assessment of collapse risk where the structure is in the severe post-elastic region [Haselton and Baker, 2006]. Such an IM is more informative as the structure accumulates damage and softens, causing the effective period to elongate considerably. Whereas for tall, long-period buildings, higher modes of vibration can significantly influence the IDR response. Therefore, an IM with a definition capable of capturing information at spectral ordinates less than the fundamental period may be more informative for IDR prediction. [Luco and Cornell, 2007]. In addition to the building's dynamic characteristics, the treatment of the physical building configuration also affects the appropriateness of the chosen IM. For relatively regular buildings, the structural response is often quantified by simplifying the 3D building into its two main orthogonal components with

2D models, and the seismic demand is determined with some form of combination (SRSS, *et cetera*). However, as shown in recent studies [Kohrangi *et al.*, 2016; 2018a], the response prediction of 3D structural models under bi-directional excitation using an IM capable of capturing information of each ground motion component can result in an increased response resolution. This is particularly true for buildings with well-separated periods between the two orthogonal directions where a scalar IM that indiscriminately combines information unique to both directions can enhance the response prediction power. This increase in response resolution can be further increased if the information is kept separate using a vector IM. The same effect can be seen for structural configurations in which the response in one direction is correlated with the excitation in the orthogonal direction, such as asymmetric buildings exhibiting torsional behaviour.

The last aspect considered in this study that makes the IM's quality unique to the particular problem of interest is the building's location relative to the influential seismic sources and the nature of the seismic hazard that the building is exposed to. For example, the presence of large forward directivity velocity pulses and other directivity effects will likely reduce the predictive power of simpler IMs such as $Sa(T_1)$. However, improvements can be made with the adoption of a more complex IM to condition the structural response. For instance, for sites where ground motion velocity pulses are important, it has been shown that a significant improvement in the predictability of structural response can be made if the characteristics of the velocity pulse are accounted for within the IM definition. This is often achieved with the implementation of a vector IM that accounts for the period of the velocity pulse or the spectral shape in addition to $Sa(T_1)$ [Baker and Cornell, 2008], which leads to the importance of spectral shape.

The spectral shape is a key characteristic of a ground motion as it gives an indication of many influential properties of the causal event. Numerous studies have shown the importance of accounting for the spectral shape in response assessment [Baker and Cornell, 2005; Haselton *et al.*, 2011; Zareian and Krawinkler, 2007; Baker and Cornell, 2006a] however, this characteristic is often not well quantified [Haselton and Baker, 2006]. The spectral shape can be accounted for within the definition of a vector IM with the addition of the parameter ε. Where ε is computed as the difference between the spectral ordinate of $lnSa(T_i)$ of the ground motion and the mean $\overline{lnSa}(T_i)$ as computed by the GMPE, standardised by the logarithmic standard deviation of the GMPE. That is, ε is a measure of how far the logarithm of a spectral ordinate of the ground motion is from median value as predicted by the GMPE, as a multiple of $ln(\sigma_{IM|rup})$. Therefore ε is dependent on the site considered, the conditioning spectral period T_i, and the GMPEs used in the PSHA calculations, but it is also dependent on the hazard level. For example, a positive ε ground motion indicates a higher than expected spectral acceleration at the conditioning period, but as the adjacent spectral ordinates are correlated, they too are likely above the expected value, and hence the positive ε value indicates that the spectral shape has a peak at this conditioning period. The opposite can be said about negative ε valued ground motion records. Therefore, ε can be used as a proxy for spectral shape in the vicinity of the conditioning period.

Given that the response of a nonlinear MDOF system is affected by periods above and below the fundamental period, it is intuitive why the spectral shape of a ground motion is so important for response prediction. In fact, it has been shown that when ε is conditioned in the vicinity of the spectral ordinates that dominate the structural response, ε has a more significant effect on the response than the causal earthquake magnitude and source to site distance [Baker and Cornell, 2005]. For example, consider two ground motion records, one being ε neutral and the other with $+2\varepsilon$, both scaled to a common intensity target of $Sa(T_1) = im$. As the positive ε record has a spectral peak at T_1, when scaled to the target, the intensity of the ground motion in the vicinity of T_1 will be less than that of the ε neutral ground motion and, hence the ε neutral ground motion will tend to cause a larger response. By disaggregating the hazard for $Sa(T_1)$ with respect to ε at different return periods, it can be seen that for frequent intensity levels $\varepsilon \leq 0$ and for rare intensity levels $\varepsilon > 0$. Therefore, if the spectral shape of the ground motion is not considered in either the definition of the IM or the record selection process, it is likely that the structural response will have a greater dispersion, and a degree of bias may be systematically introduced as the return period of the conditioning IM is increased. This is particularly true when analytical data is obtained using the incremental dynamic analysis method, where a single set of ground motions are used to estimate the response over a wide spectrum of intensity levels.

Given that the relationship between the ground motion characteristics and the structural response is highly complex, it is not surprising that a single scalar IM is unlikely to capture all relevant characteristics of the ground motion that influence the structural response [L. Eads, E. Miranda and D. Lignos, 2015]. As alluded to above, this motivates the adoption of a more sophisticated vector IM that is conditioned on carefully selected ground motion characteristics that dominate the structural response. Such an IM is more likely to produce a response that is conditionally independent of all other characteristics not directly captured by the vector IM definition. It has been shown that when the response is conditioned on a vector IM, the efficiency of the structural response prediction can be improved, and the bias introduced by a relatively insufficient scalar IM can be at least be partially removed [Baker and Cornell, 2005; Kohrangi *et al.*, 2016]. Unfortunately, when using the more sophisticated vector IM, the computation of MAF$_{LS}$ quickly becomes cumbersome as all elements in the computation become significantly more complicated; including vector PSHA [VPSHA: Bazzurro and Cornell, 2002] and a fragility function now defined by an $n_{im} + 1$ dimensional surface, making results difficult to visualise when more than two IMs are included in the vector. Thankfully, it is possible to mitigate the potential inadequacies of the simpler scalar IM with careful record selection that enables other influential ground motion characteristics to be captured. For instance, it has been found that when selecting records with a spectral shape consistent with the hazard, the reduction in the variance and the degree of bias introduced in the resulting response distribution is comparable to the reductions achieved by using a vector-valued IM including ε [Baker and Cornell, 2006a].

The classical intensity measure of the spectral acceleration at the fundamental period of the structure, $Sa(T_1)$, is perhaps the most familiar intensity measure used by many engineers to link the hazard to the structural response. The IM of $Sa(T_1)$ has a clear definition, is easily quantified and is a perfect predictor of the structural response of an elastic SDOF system with a fundamental period of T_1. However, several studies have demonstrated that $Sa(T_1)$ may not be

particularly efficient nor sufficient for some structures [Luco and Cornell, 2007] and based on the discussion above, it should be no surprise that several IMs have been shown to outperform Sa(T$_1$) [Kohrangi *et al*., 2016]. Many researchers have found that an IM quantified by averaging spectral acceleration ordinates over a period range can be a significantly more efficient predictor of displacement-based nonlinear structural response, and it is also more likely to be sufficient [L. Eads, E. Miranda and D. Lignos, 2015]. Both IMs are defined with the peak response of a linear elastic SDOF system with characteristics quantified by the structures initial conditions. However, $Sa(T_1)$ does not directly account for the elastic response at periods less than the fundamental mode of vibration, which dictate the response of the higher modes. Furthermore, $Sa(T_1)$ lacks the ability to account for the relevant response once the structure moves past the elastic limit and accumulates damage, causing period elongation as the structure softens. In comparison, the IM defined by the average of spectral ordinates, Sa_{ave}, is able to simultaneously account for the relevant information that is influential for both the higher mode response and changes in the dynamic characteristics caused by the ductility demand.

In a study on the efficiency and sufficiency of Sa_{ave} compared to $Sa(T_1)$ it was found that both IMs were sufficient with respect to the source to site distance. However, the sufficiency of Sa_{ave} with respect to magnitude reduced with reducing first mode period of the structure to the point where $Sa(T_1)$ was more sufficient for structures with periods less approximately 1.2s. This result was considered to be related to the portion of the spectral peak within the period range used to define Sa_{ave} and sufficiency improvements can be made by refining the window used to compute Sa_{ave} [L. Eads, E. Miranda and D. Lignos, 2015]. The sufficiency with respect to earthquake magnitude can also be improved with careful record selection to address this potential issue. Additionally, for first mode dominated structures responding with low ductility demand, $Sa(T_1)$ is likely to outperform the more sophisticated IM of Sa_{ave} due to its ability to target the most influential spectral ordinate. However, due to the inability of $Sa(T_1)$ to capture the spectral shape, even for such structures, Sa_{ave} is more likely to predict accurate response for sites influenced by near-field effects [Kohrangi *et al*., 2018b].

As discussed in [Kohrangi *et al.*, 2016], the definition of the average spectral acceleration as the conditioning IM can be tailored to better capture the distribution of the IDR, to the detriment of PFA, by defining the IM with more weight towards spectral ordinates longer than the first mode period. Furthermore, if the average spectral acceleration is defined as the geometric mean of these ordinates, as opposed to the arithmetic mean, the resulting IM is less sensitive to extreme spectral values. More importantly, adopting the geometric mean permits the use of existing GMPEs that provide the expected value and standard deviation of each spectral ordinate, such that the expected value and standard deviation of IM = $\ln(Sa_{ave,g.m})$ can be estimated. Therefore, $\lambda_{Sa,ave}(x)$ can be computed with the use of existing GMPEs and existing correlation equations for the relationship between spectral acceleration values. Although determining the hazard for Sa_{ave}, is not as practical as Sa(T1), the IM of Sa_{ave} has lower conditional variability and therefore $\sigma_{\ln (sa,ave)|rup}$ is less than $\sigma_{\ln (sa(T1))|rup}$, hence Sa_{ave} can be predicted with greater confidence. This is due to the averaging operation used in the computation of Sa_{ave} and the fact that the correlation coefficients for spectral acceleration at adjacent periods are not that significant.

Because of the ability of Sa_{ave} to address many of the aspects discussed above while maintaining a suitable balance between practicality and accuracy, the average spectral acceleration is adopted as the conditioning IM to link the hazard to the structural response. The specific definition of Sa_{ave} adopted is the geometric mean of the elastic response spectra with 5% equivalent viscous damping, calculated with Equation 3.3.

$$Sa_{ave} = \left(\prod_{i=1}^{n} Sa(T_i) \right)^{1/n} \tag{3.3}$$

Where the spectral ordinates of $Sa(T_i)$ are the geometric mean of both horizontal components of the ground motion, rather than the ordinates of an arbitrary component. In an attempt to capture the higher mode response and period elongation effects of the building considered, Sa_{ave} is computed with 31 linearly spaced spectral ordinates, with the lower bound of the period range set to the second mode period and an upper bound set at approximately 2.5 times the effective first mode period as estimated by the pushover analysis. This results in the period window used to compute Sa_{ave} of 0.1s to 3.1s with an increment of 0.1s.

3.3 Efficient Fragility Computation

Having decided on an intensity measure to represent the severity of a ground motion, a method must be established to link this intensity measure to the probability of exceeding a given structural response in the form of a fragility function. There are a number of approaches for collecting the required data from the results of the response analyses to estimate a fragility function. A popular method, particularly for collapse assessment, is incremental dynamic analysis [IDA: Vamvatsikos and Cornell, 2002], where the structure's response is measured for a suite of ground motions with their intensity incrementally increased until the required data is obtained from each ground motion. The IDA approach uses the same record set, often arbitrarily selected, to represent the characteristics of the hazard at all intensity levels considered. However, ground motion characteristics are dependent on the hazard level as frequent, low intensity ground motions are generally associated with different causal magnitudes and distances than the larger, rarer intensities. More importantly, there are significant changes in the characteristic spectral shape as the intensity level increases, as discussed in Section 3.4.

Another common approach for data collection is multiple stripes analysis [MSA: Jalayer, 2003], where the structural response is obtained at a set of predefined IM levels. Unlike IDA, using the MSA procedure allows for a unique set of records to be selected at each intensity level. Therefore, the MSA method provides the opportunity to capture other ground motion characteristics not directly captured within the definition of the conditioning IM; such as the importance of spectral shape. This ability to tailor the record selection as the intensity level changes provides better fidelity to the hazard and is the reason why MSA is the adopted method for this study.

To estimate the fragility functions, the random variable of the MIDR, given a ground motion intensity level of $IM = x$, and non-collapse C' is assumed to be adequately described by the lognormal distribution, as is commonly done. Therefore, using the standard normal cumulative distribution function $\Phi(\cdot)$ the probability of exceeding any arbitrary MIDR threshold z, under the aforementioned conditions can be determined using Equation 3.4.

$$P(MIDR > z|IM = x, C') = P(C'|IM = x) \cdot \left(1 - \Phi\left(\frac{ln(x/\hat{\theta})}{\hat{\beta}} \right) \right) \qquad (3.4)$$

Where, $P(C'|IM = x)$ is simply the ratio of ground motions not causing collapse to the total number of ground motions, at each intensity level $IM = x$. The median and dispersion the of fragility function are denoted as $\hat{\theta}$ and $\hat{\beta}$ respectively to distinguish the estimates obtained with the limited number of response analyses from the true distribution parameters, θ and β. Where $\hat{\theta}$ defines the IM level that produced 50% of the response analyses to exceed the limit state drift threshold and $\hat{\beta}$ is the standard deviation of $lnIM$. Applying the total probability theorem, the characterisation of both the collapse and non-collapse data obtained with the response analyses can be combined to produce the total probability of exceeding a MIDR threshold z as defined by Equation 3.5.

$$P(MIDR > z | IM = x) = P(C | IM = x) + P(C' | IM = x) \cdot \left(1 - \Phi\left(\frac{ln(x/\hat{\theta})}{\hat{\beta}}\right)\right) \qquad (3.5)$$

Where $P(C \mid IM = x)$ is the complement to $P(C' \mid IM = x)$. By substituting the assumed fragility function form into Equation 3.2, the MAF$_{LS}$ can now be computed using Equation 3.6.

$$\lambda(MIDR > z) = \int_0^{+\infty} \left(P(C | IM = x) + P(C' | IM = x) \cdot \left(1 - \Phi\left(\frac{ln(x/\hat{\theta})}{\hat{\beta}}\right)\right) \right) \cdot |d\lambda_{IM}(x)| \qquad (3.6)$$

As the structural response is obtained at discrete IM levels with the MSA method, the IM level of each ground motion associated with the onset of exceedance of the limit state drift threshold is unknown. Therefore, the maximum likelihood method will be adopted to determine $\hat{\theta}$ and $\hat{\beta}$ by utilising the fraction of ground motions causing a response greater than the specified drift limit at each IM level, given non-collapse. The likelihood function to be maximised is given by Equation 3.7 [Baker, 2015], which is formulated using the lognormal cumulative distribution function and by assuming the observations are independent.

$$Likelihood = \prod_{j=1}^{m} \binom{n_i}{z_j} \Phi\left(\frac{\ln(x/\hat{\theta})}{\hat{\beta}}\right)^{z_j} \left(1 - \Phi\left(\frac{\ln(x/\hat{\theta})}{\hat{\beta}}\right)\right)^{n_j - z_j} \qquad (3.7)$$

Where the maximum likelihood method determines $\hat{\theta}$ and $\hat{\beta}$ such that the resulting fragility function produces the highest probability of having observed the z_j exceedances out of n_j records across the entire data set that covers m IM levels. As no effort will be taken to ensure that unique records are selected for each IM level, the observations may not be strictly independent, as assumed by the formulation given by Equation 3.7. However, as discussed by Baker [2015] this potential lack of independence is unlikely to affect the estimated fragility curve parameters.

3.4   Hazard Computation and Record Selection

3.4.1   Hazard Analysis

A probabilistic seismic hazard analysis was performed at the three sites in Athens, Perugia and Focsani with specific coordinates given in Table 2.1 to predict the occurrence of the conditioning intensity measure, $\lambda_{Sa_{ave}}(x)$. The hazard and disaggregation computations were performed by Kohrangi [2019] using OpenQuake [Monelli *et al.*, 2012], an open-source software for seismic hazard and risk assessment developed by the Global Earthquake Model (GEM) organization. All seismic sources within 200 km of each site were considered, and the computations used the SHARE area source model with the Boore and Atkinson [2008] ground motion prediction equation. The analysis assumed a shear wave velocity in the top 30 m of V_{s30}=360 ms^{-1}; consistent with the design assumption. For each site, the uniform hazard spectrum (UHS) was computed for the design intensity with 10% probability of exceedance in 50 years (10/50) and compared to the EN1998 Type 1 (EC8) design spectrum. The result is shown in Figure 3.1 where again the design spectrum has been produced by continuing the constant velocity region of the response spectrum into the constant displacement region as discussed in Section 2.1.
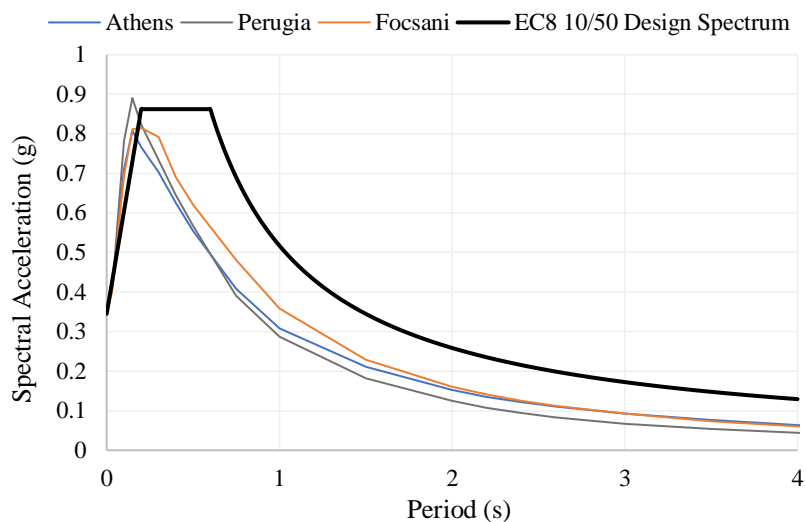

Figure 3.1 Comparison between the 10/50 UHS to the EC8 design spectrum

It can be seen by the comparison in Figure 3.1 that at the effective period ($T_e = 2.2$ s) governing the required base shear, the design intensity is 1.74, 2.19 and 1.67 times more severe than the actual hazard of the three sites of Athens, Perugia and Focsani, respectively. Therefore, the building performance is influenced by two variables; the effect of hazard inconsistency with the EC8 design spectrum and the effect that the DDBD method has on the building performance. In an attempt to isolate the latter, an additional set of hazard curves have been produced for the three sites by uniformly scaling the annual rate of exceedance of each spectral ordinate such that the resulting UHS matches the design intensity at $T_e = 2.2$ s. Adopting assumptions consistent with the design procedure in Section 2.1, displacement response spectra are generated from the scaled UHS of each site and compared to the inelastic displacement response spectra used in the design. The comparison is presented in Figure 3.2.
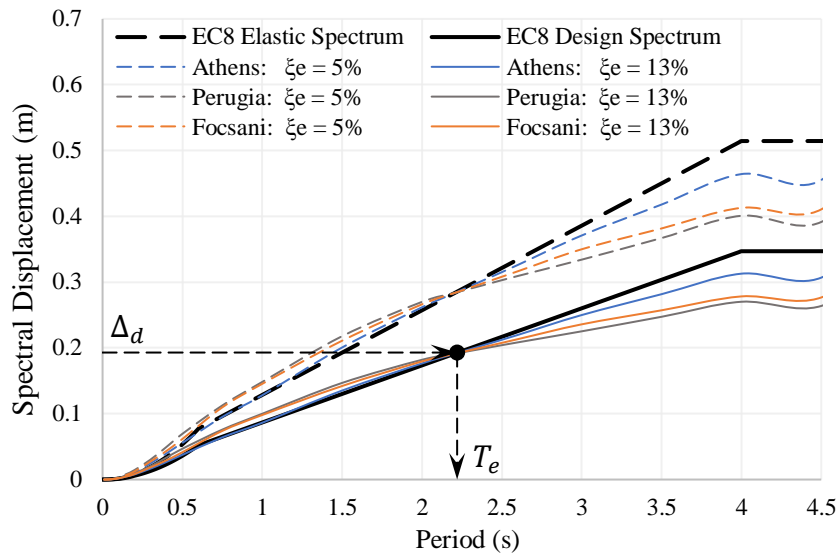
Figure 3.2 Comparison of scaled UHS to design spectrum

This method of hazard scaling is akin to altering the base rate $\lambda_{0,i}$ given in Equation 3.1 to increase the hazard while maintaining the causal distributions of magnitudes and distances that are characteristic of the three sites. Therefore, the relative contributions to the hazard from different earthquake scenarios are identical for both sets of hazard curves and hence records selected utilising the disaggregation results are equally representative. By convolving the two sets of hazard curves shown in Figure 3.3 with the fragility functions produced from the MSA results, both the variation in the performance as seen by a practitioner and due to the performance of the DDBD method itself can be estimated.
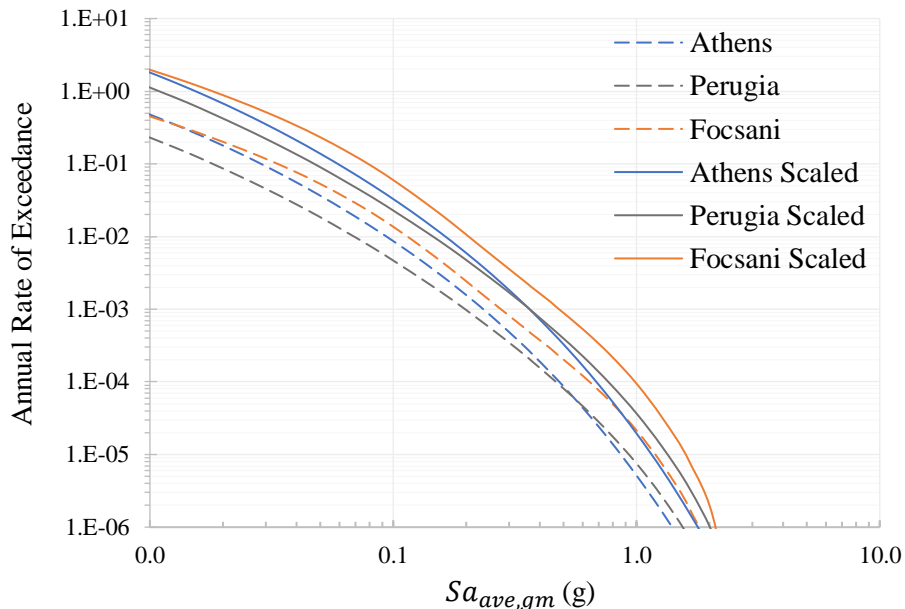

Figure 3.3 Seismic hazard curve comparison

3.4.2 *Hazard Disaggregation*

To inform the record selection process, the hazard was disaggregated at ten intensity levels, $Sa_{ave} = x_i$, to identify the relative contributions to the hazard from different earthquake scenarios. To achieve this, the hazard was disaggregated with respect to the causal magnitude, source to site distance and ε, to obtain the joint probability mass function (PMF) conditioned on the exceedance of the intensity levels, $Sa_{ave} > x$, given in Table 3.1. The resulting PMFs for each site are shown in Figure 3.4, which describes how much each scenario contributes in the numerical integration producing the total annual rate of exceeding each intensity level, $Sa_{ave} > x_i$. It can be argued that hazard disaggregation with respect to the exceedance of the conditioning intensity level is more appropriate for conventional response history analysis where the performance is estimated at an intensity with a specific return period (e.g. 475-year return period for ULS). Whereas disaggregation with respect to the occurrence of the conditioning intensity level is more appropriate for the following risk assessment where the response is estimated at discrete intensity levels $Sa_{ave} = x$. Due to the fact that exceedance disaggregation has a greater contribution from events with larger magnitudes and shorter distances with respect to occurrence disaggregation, the resulting conditional spectra can produce conservative estimates of the expected ground motion for a given rate of occurrence. However, as shown by Fox *et al.* [2016], as the frequency of the ground motion intensity decreases, most rupture scenarios require positive epsilon values to contribute to the hazard for both the exceedance and occurrence case. As a consequence, the resulting distributions are similar. As will be seen in Chapter 4, the building's response at the level of interest is controlled by relatively high-intensity levels, and therefore the difference between the two methods is unlikely to be significant. Furthermore, conditional spectra can be computed by back calculating ε values to reproduce the exact IM levels given in Table 3.1.

Table 3.1 Disaggregated intensity levels

| PoE (%) in 50 years	λ (MAR)	Return period	Intensity, Sa_{ave}		
			Athens	Perugia	Focsani
70	2.4×10^{-02}	42	0.062	0.043	0.077
50	1.4×10^{-02}	72	0.081	0.058	0.099
30	7.1×10^{-03}	140	0.109	0.082	0.132
10	2.1×10^{-03}	475	0.179	0.144	0.210
5	1.0×10^{-03}	975	0.232	0.195	0.274
2	4.0×10^{-04}	2475	0.317	0.282	0.388
1.5	3.0×10^{-04}	3308	0.348	0.314	0.432
1	2.0×10^{-04}	4975	0.393	0.366	0.502
0.6	1.2×10^{-04}	8308	0.457	0.438	0.602
0.2	4.0×10^{-05}	24975	0.616	0.627	0.844

The binning scheme adopted uses uniform increments for both magnitude and ε of $\Delta m = 0.5$ and $\Delta \varepsilon = 1.0$. The bin width of the source to site distance has been varied as the ground motion characteristics change appreciably for shorter distances, whereas events occurring at larger distances are often perceived as equally distant from the site [Bazzurro and Cornell, 1999]. To capture this effect in the ground motion selection procedure, the bin width for source to site distance has been increased from $\Delta r = 15$ km for R $\leq$ 30 km up to $\Delta r = 100$ km for R >100km.
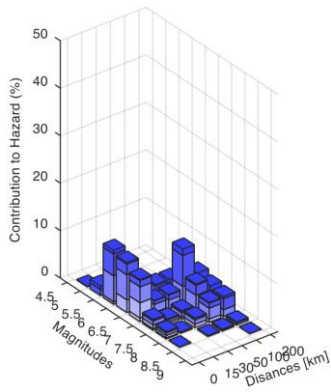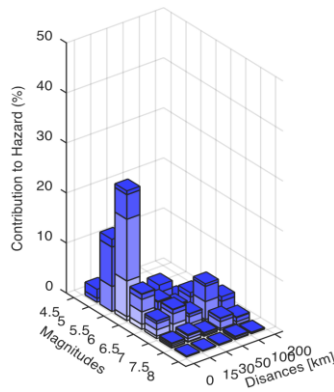
Athens **Perugia** **Focsani**
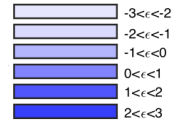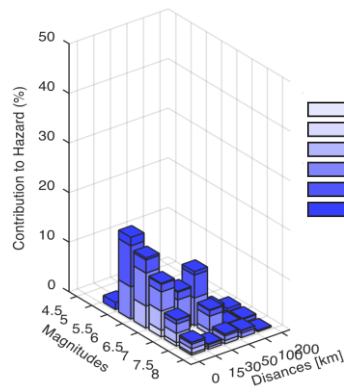
IM Level 1: 70% PoE in 50 years
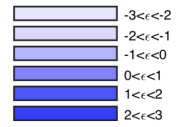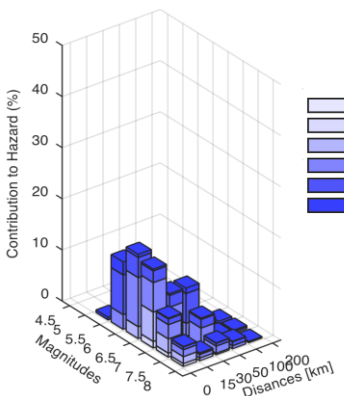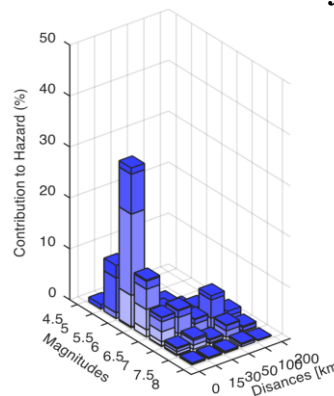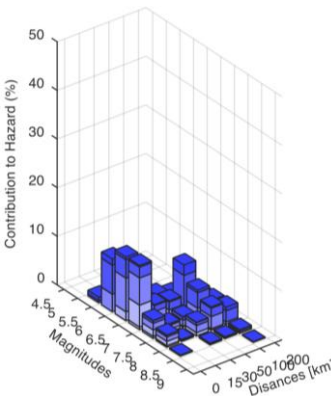
IM Level 2: 50% PoE in 50 years
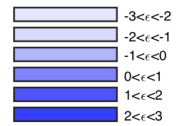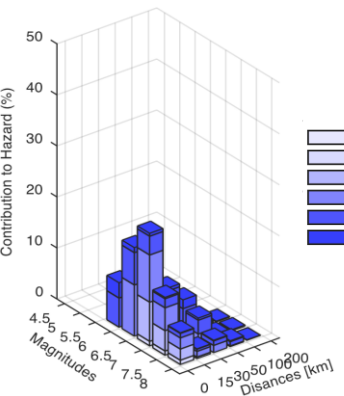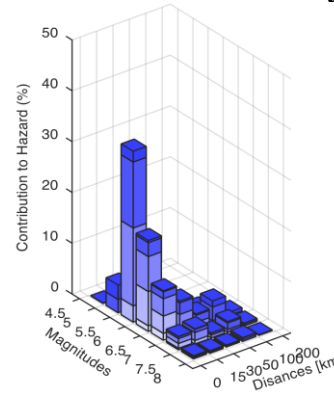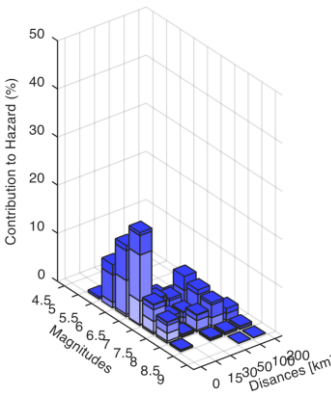
IM Level 3: 30% PoE in 50 years
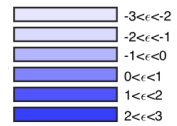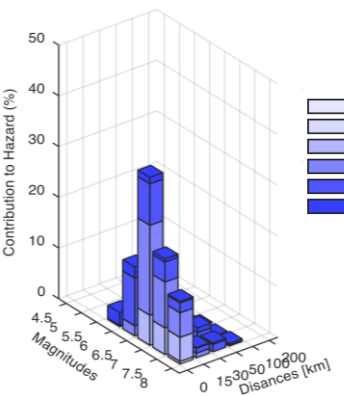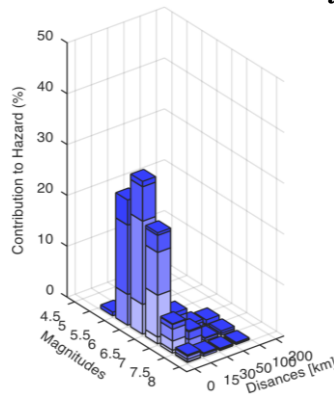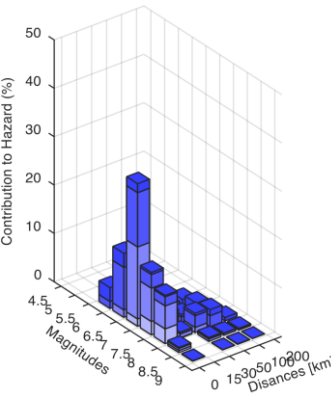
IM Level 4: 10% PoE in 50 years
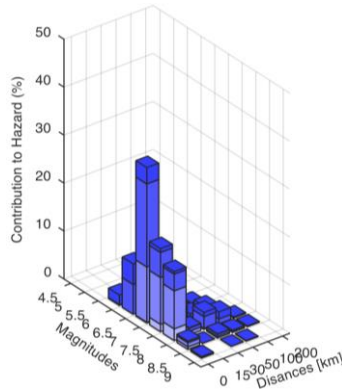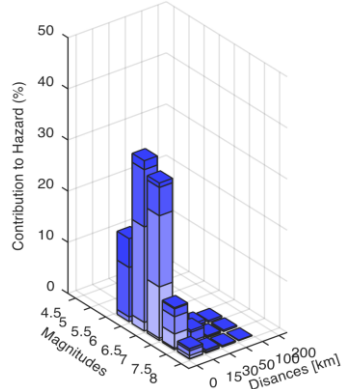
Athens **Perugia** **Focsani**
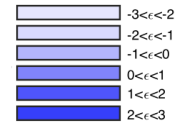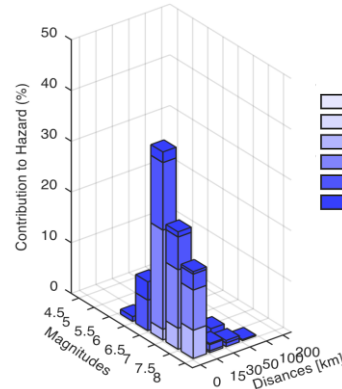
IM Level 5: 5% PoE in 50 years
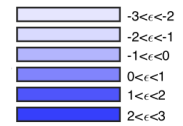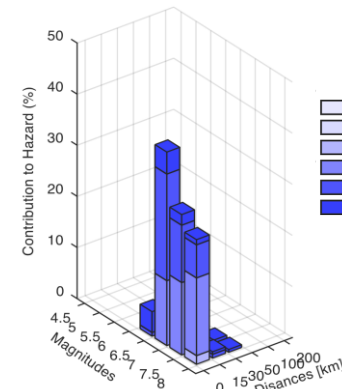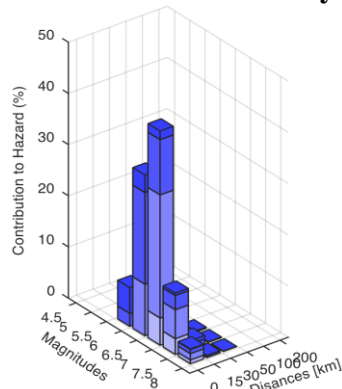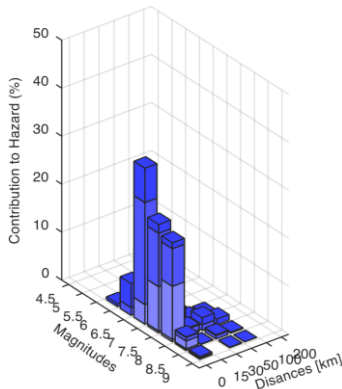
IM Level 6: 2% PoE in 50 years
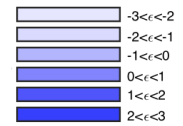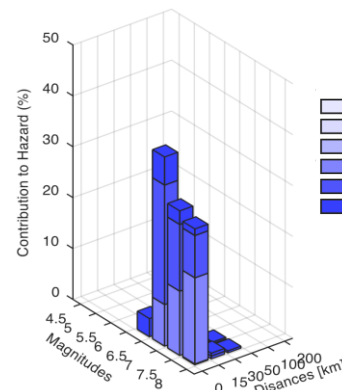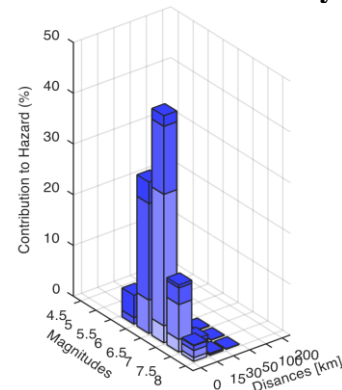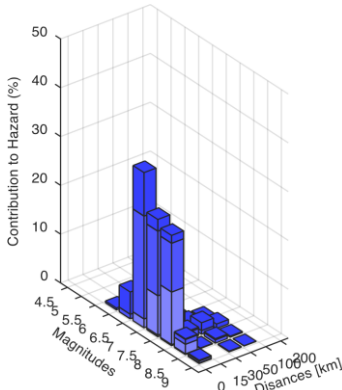
IM Level 7: 1.5% PoE in 50 years
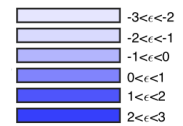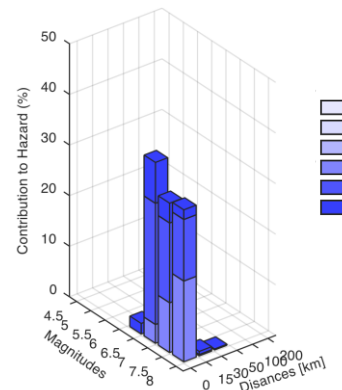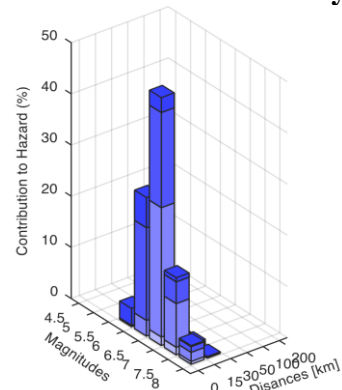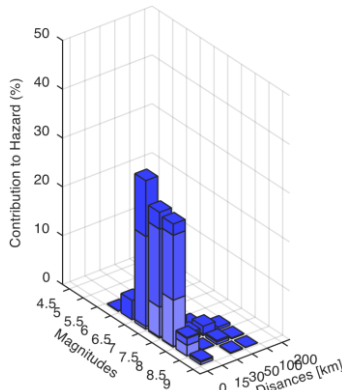
IM Level 8: 1.0% PoE in 50 years

Athens   **Perugia**   **Focsani**

IM Level 9: 0.6% PoE in 50 years

IM Level 10: 0.2% PoE in 50 years
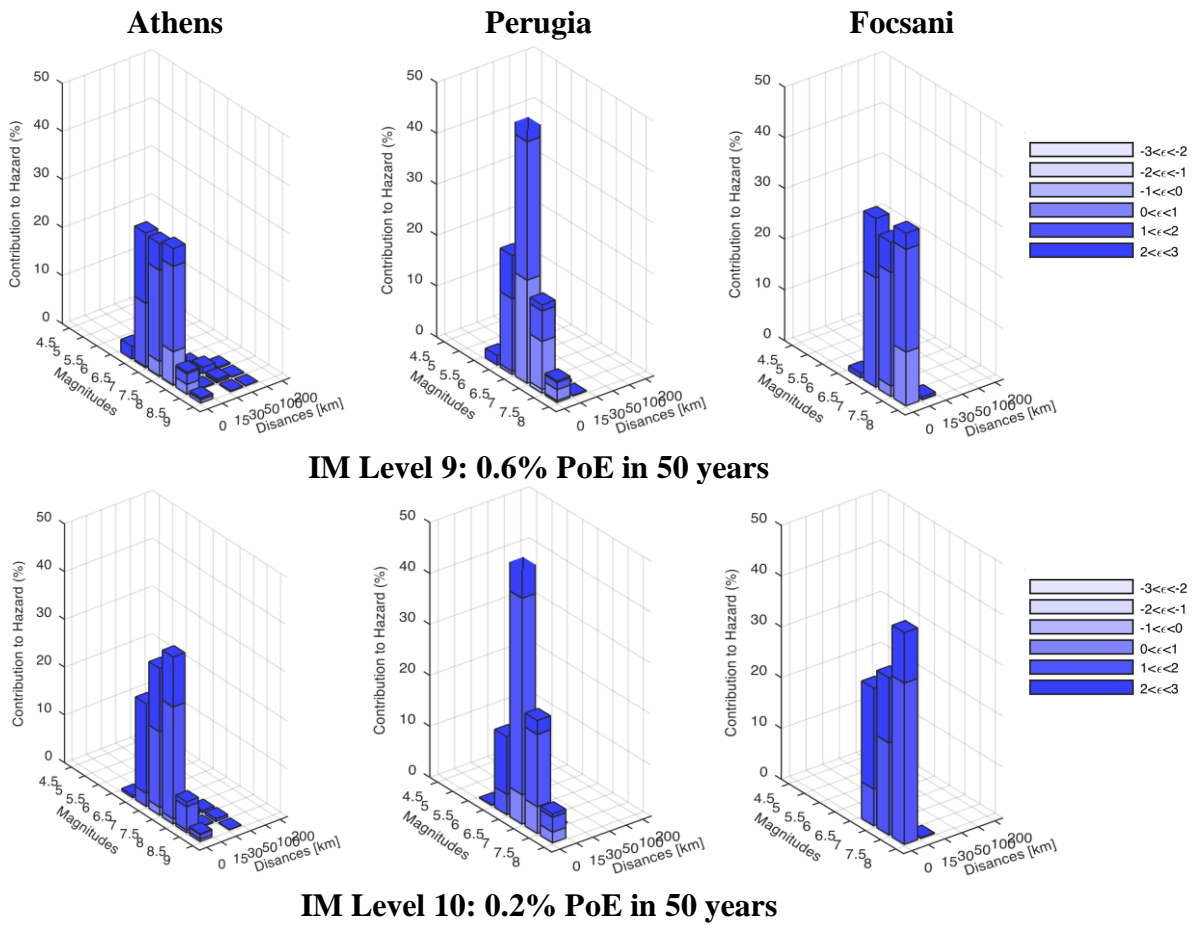
Figure 3.4 Site disaggregation PMF conditioned on the exceedance of $Sa_{ave} > x$

3.4.3   Ground Motion Selection and Scaling

The method adopted for the record selection process is focused on the accurate estimation of the structural response distribution for each intensity level considered. With a careful record selection procedure, the sufficiency of the estimated response can be improved by compensating for the inadequacies of the relatively simple scalar IM. This can be achieved by selecting hazard consistent earthquake ground motions that represent influential characteristics at each intensity level that are not directly accounted for within the definition of the conditioning IM.

It can be seen by the hazard disaggregation results in Figure 3.4 that the distribution of the causal magnitudes M, source to site distances R, and ε values can vary considerably between the three sites and the intensity level of interest. It is therefore desired to select a record set for each intensity level, unique to each site, that reflect these changes in the ground motion characteristics. This can be achieved by populating the record set with ground motions of causal magnitudes, distances and ε values in proportion to their relative contributions to the hazard. The selection criteria can be extended to limit ground motions to represent other characteristics such as soil conditions or the contributing fault rupture mechanism. However, given the finite number of recorded ground motions, simultaneously matching the target distribution of all parameters can be difficult in practice, and therefore, priority should be given to matching the most influential ground motion characteristics. For example, as previously mentioned, careful record selection can provide the opportunity to account for the important ground motion property of spectral shape using ε as a proxy. Furthermore, it has been shown that both the causal magnitude and source to site distance are of secondary importance to the spectral shape and therefore accurately representing the distribution of ε values should be prioritised at the expense of relaxing the accurate representation of M and R [Baker and Cornell, 2005; 2006a].

After scaling representative ground motions to the required intensity level, records can then be selected based on their similarity over a period range with a target response spectrum that is derived from the PSHA results. A target spectrum that is commonly adopted is the uniform hazard spectrum (UHS). The UHS is computed by performing PSHA calculations to produce independent hazard curves for spectral acceleration at several periods and collecting the intensity of spectral ordinates corresponding to a target exceedance rate. The resulting locus of points produces an acceleration spectrum with all ordinates having an equal rate of being exceeded. However, as discussed by Baker and Cornell [2006a], the high-frequency portion of the UHS is generally dominated by frequent events close to the site and the low-frequency portion of the UHS is generally dominated by infrequent events at larger distances from the site. Consequently, the shape of the UHS can be very different to the shape of the expected response spectrum of a real ground motion having an equally high spectral amplitude at a given period [Baker, 2005; Haselton and Baker, 2006; Haselton *et al*., 2011]. Because the UHS is derived from the many contributing events, no realistic ground motion will produce a response spectrum as high as the UHS at all periods. Therefore, modifying ground motions to match the UHS as a target spectrum will produce a conservative upper bound of the seismic risk estimate. The UHS is more suited for design purposes at hazard levels corresponding to distinct limit states. However, the conditional mean spectrum (CMS) or the conditional spectrum (CS) are superior alternatives for obtaining unbiased seismic risk estimates.

The CMS method utilises the disaggregated earthquake rupture scenarios of M, R and ε that are conditioned on the exceedance of a target intensity measure, to estimate the mean acceleration response spectrum, $\mu_{lnSa(T_i)|lnSa_{ave}=x,rup}$. The CS expands the CMS to account for the entire conditional distribution of spectral acceleration by incorporating the conditional variation about the mean, $\sigma_{lnSa(T_i)|lnSa_{ave}=x,rup}$. In this study, the exact CS [Lin *et al.*, 2013] method is adopted for record selection, conditioned on the exceedance of the average spectral acceleration levels given in Table 3.1 above [Kohrangi *et al.*, 2017]. Unlike the UHS, where the occurrences of the spectral ordinates are independent, the adopted conditional spectrum approach incorporates the Baker and Jayaram [2008] correlation relationship, $\rho_{lnSa(T_i),lnSa_{ave}}$, for spectral acceleration values across periods to estimate the expected response spectrum using M, R, and ε values only as proxies for spectral shape. Hazard consistent ground motions can then be selected such that the statistics of the ground motion suite replicate the statistics of the hazard determined by the conditional mean and standard deviation given by Equations 3.8 and 3.9, respectively. That is, record selection is purely based on the intensity-dependent spectral shape rather than the record's actual M, R and ε values. This is likely to increase the number of suitable records to be selected as more records are likely to have the required spectral shape than the correct combination of M, R and ε values.

$$\mu_{lnSa(T_i)|lnSa_{ave}=x,rup} = \mu_{lnSa(T_i)|\,rup} + \rho_{lnSa(T_i),lnSa_{ave}} \cdot \sigma_{\ln Sa(T_i)|rup} \cdot \varepsilon_{lnSa_{ave}|rup} \qquad (3.8)$$

$$\sigma_{lnSa(T_i)|lnSa_{ave}=x,rup} = \sigma_{\ln Sa(T_i)|rup} \cdot \left(1 - \rho^2_{lnSa(T_i),lnSa_{ave}}\right)^{1/2} \qquad (3.9)$$

Where the logarithmic mean, $\mu_{lnSa(T_i)|\,rup}$, and standard deviation, $\sigma_{\ln Sa(T_i)|rup}$, of spectral acceleration at periods T_i, are determined with the Boore and Atkinson (2008) GMPE using other parameters θ, consistent with the site conditions (V_{s30}) and fault mechanisms of the rupture scenarios. As mentioned above, the hazard has been disaggregated with respect to ε with a course increment of $\Delta\varepsilon = 1.0$ to aid in the visualisation of the results presented in Figure 3.4. It is, therefore, unlikely that the exact intensity measure required will be reproduced with such a course increment. To resolve this issue, $\varepsilon_{lnSa_{ave}|rup}$ has been back calculated to produce a CS with an intensity matching the disaggregated hazard levels presented in Table 3.1. Furthermore, it can be seen by Equation 3.9 that the CS is more informed than the UHS and as a consequence, for $\rho_{lnSa(T_i),lnSa_{ave}} \neq 0$, the uncertainty in the spectral acceleration decreases, presenting another benefit of the CS method.

This approach can be extended to capture ground motion characteristics not directly represented by the acceleration response spectrum with the adoption of the generalised conditional intensity measure approach [GCIM: Bradley, 2010]. Through rigorous record selection, the GCIM approach expands the extent of hazard consistency to account for other important ground motion properties (e.g. duration or Arias intensity) by populating the record set with representative ground motions. However, such detail is not considered in this study.

The consequence of the different distributions of causal magnitudes M, source to site distances R, and ε values contributing to the hazard for the three sites are shown in Figure 3.5 below by comparing the resulting conditional mean spectrum with $\pm\, 2\sigma_{lnSa(T_i)}$ at each intensity level.
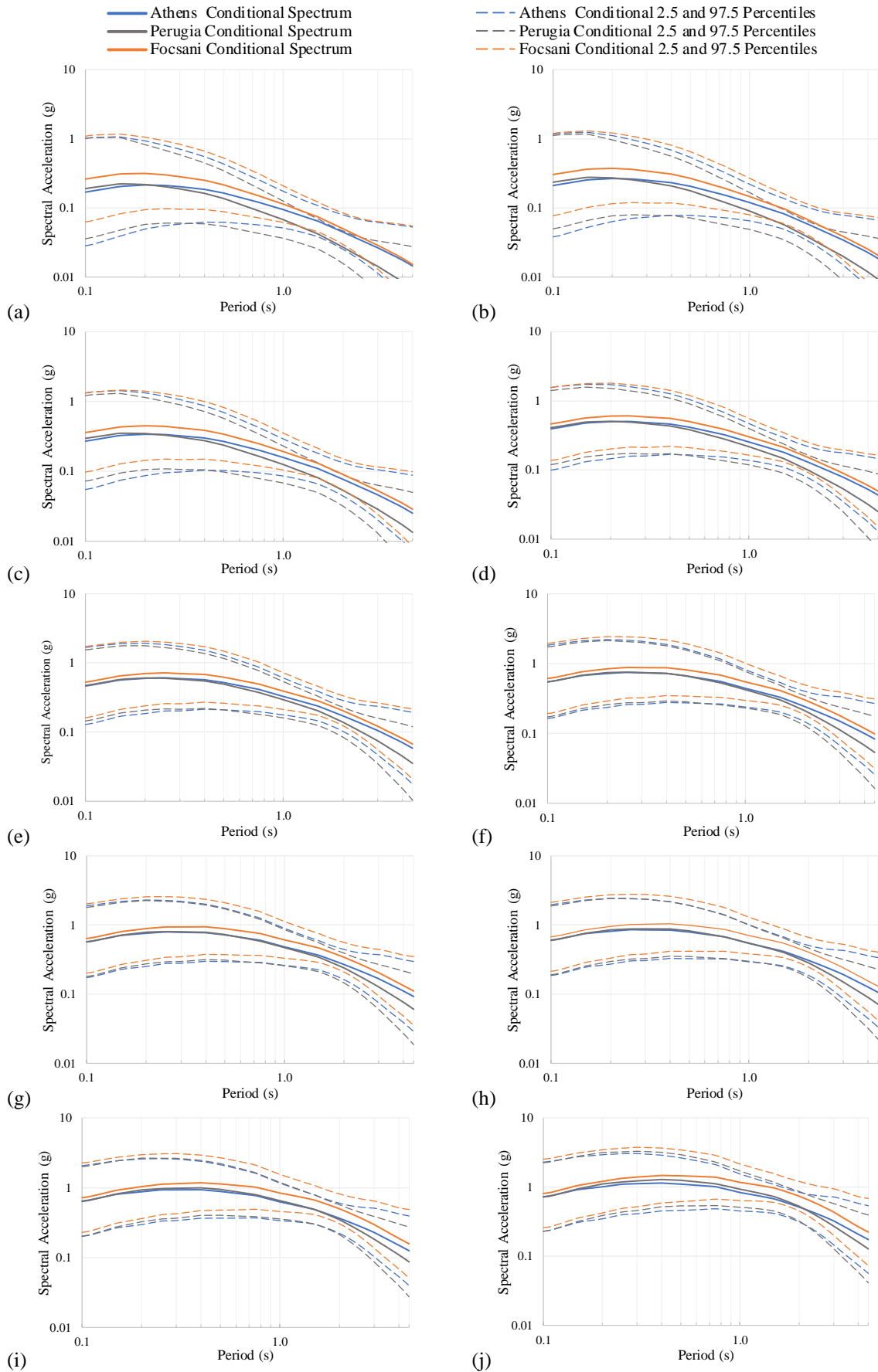
Figure 3.5 Conditional spectrum comparison between sites for IM levels 1 to 10 (a) to (j)

As shown in Figure 3.5, for a given annual rate of exceedance, the shape and intensity of the conditional spectrum are dependent, to differing degrees, on the site of interest. This is a consequence of the different causal distributions of magnitudes, source to site distances and ε values produced by the influential seismic sources surrounding each site and their relative rates of activity. Furthermore, as shown by the disaggregation results in Figure 3.4, the lower, more frequent ground motion levels are typically associated with different magnitudes and distances than higher, less frequent ground motion intensities. As a consequence, there is a proportional shift in the energy content from the higher frequencies towards the lower frequencies as the severity of the ground motion increases. The implication of this is reflected by the changing spectral shape and the resulting shift in the predominant period of the response spectra as shown in Figure 3.5.

It is, therefore, evident why it is desired to use a data collection strategy (such as MSA) that allows for a unique set of records to be selected at each intensity level to represent the aforementioned changes in hazard characteristics. For each site, 20 two-component earthquake ground motions were selected for each intensity level from the Pacific Earthquake Engineering Research Centre (PEER) Next Generation Attenuation (NGA) database [PEER, 2008]. To maintain hazard consistency [Baker and Cornell, 2006b] with respect to the definition of the conditioning IM, the records were selected based on their scaled spectral shape, computed as the geometric mean of the two ground motion components, with uniform scaling applied to each component. Only record accelerogram scaling has been employed, and the original record frequency content has been maintained. Figures 3.6 to 3.8 compare the statistics of the selected ground motion sets to the conditional mean and conditional 2.5 and 97.5 percentiles representing the hazard of the sites located in Athens, Perugia and Focsani, respectively.

The selected records shown in Figures 3.6 to 3.8 are presented in Appendix A, identified by their sequence number from the NGA database. The arbitrary component of the ground motion and the accelerogram's scale factor used in the structural response assessment are also presented in Appendix A.
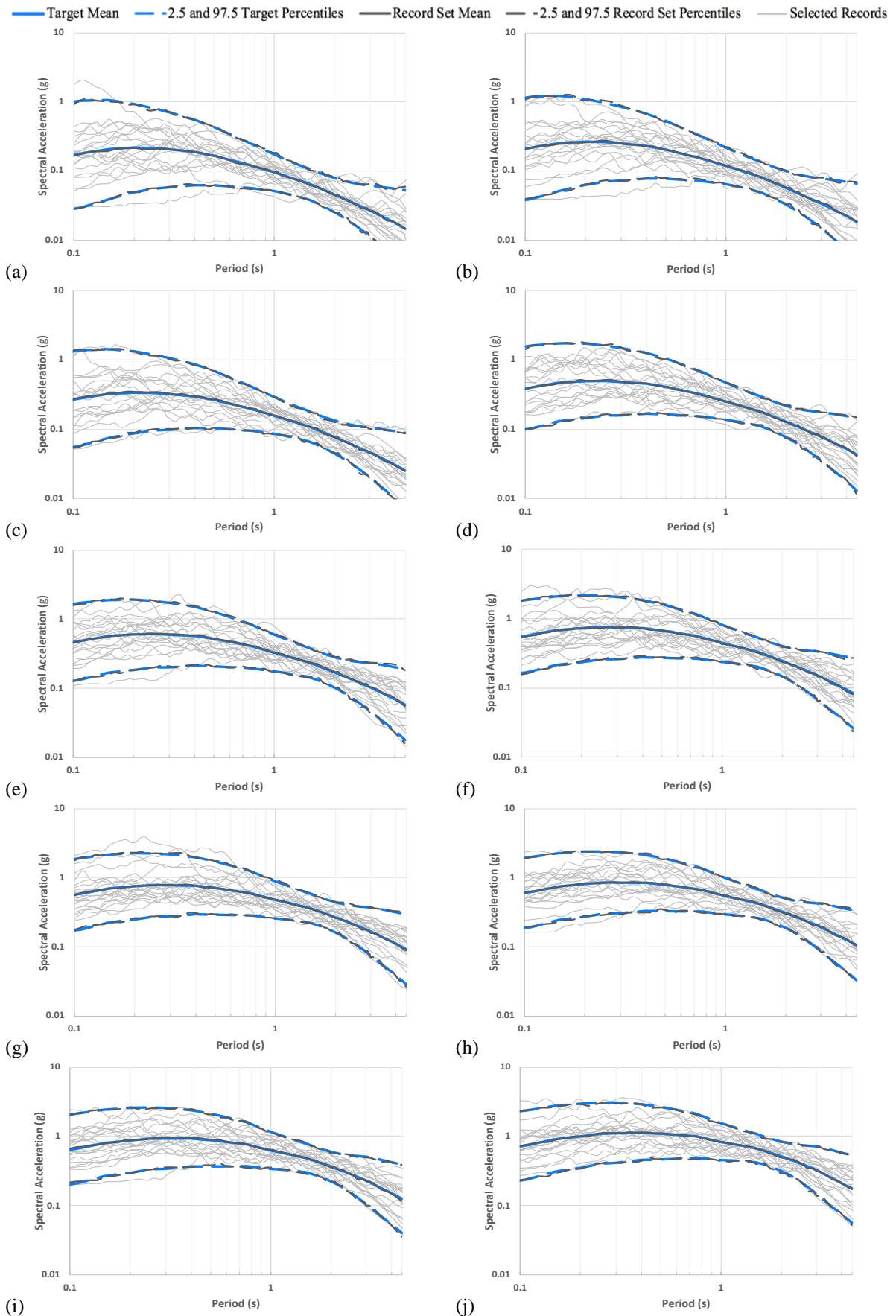
Figure 3.6 Selected records for Athens IM levels 1 to 10 (a) to (j) compared to target CS
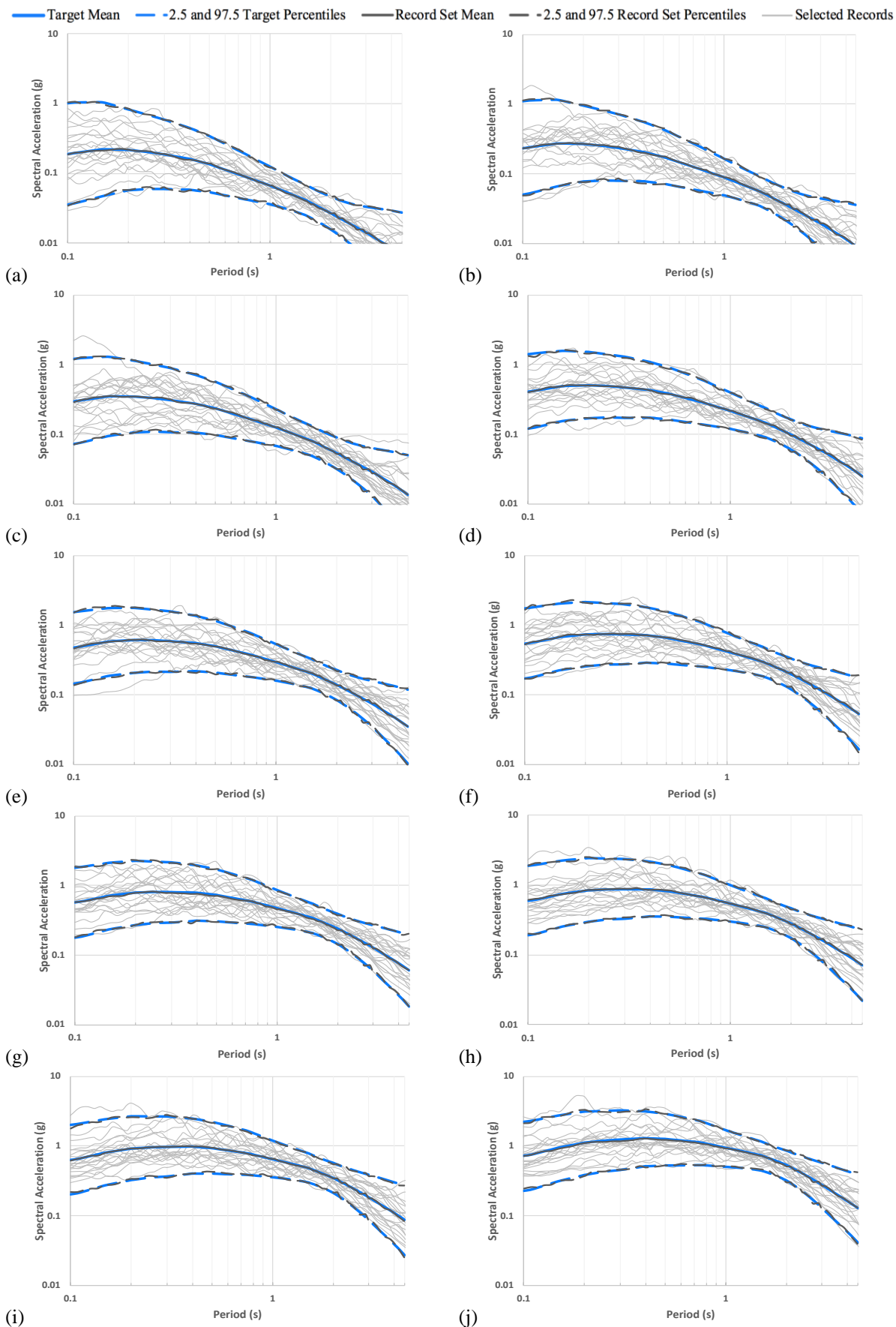
Figure 3.7 Selected records for Perugia IM levels 1 to 10 (a) to (j) compared to target CS
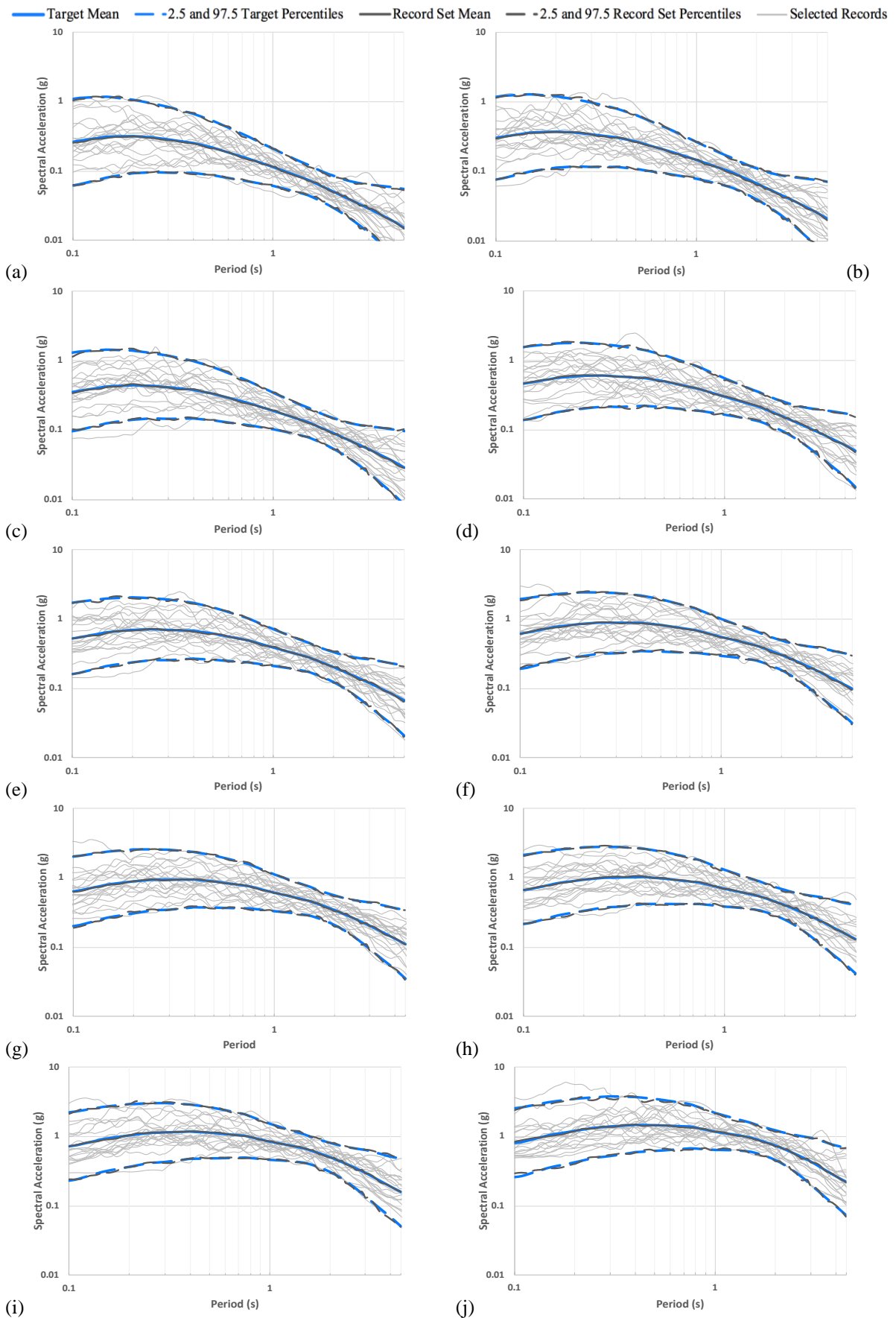
Figure 3.8 Selected records for Focsani IM levels 1 to 10 (a) to (j) compared to target CS

4 BUILDING PERFORMANCE

4.1 Multiple Stripe Analysis

The records selected in Section 3.4.3 were used to perform 200 nonlinear time-history response analyses of the same building located at each site to estimate the distribution of the random variable MIDR, given a ground motion with an intensity level of $Sa_{ave,gm}$. The analytical result of the MIDR obtained with the MSA method are shown in Figures 4.1 to 4.3 for the three sites located in Athens, Perugia and Focsani, respectively. Any MIDR result that indicated structural collapse, as defined in Section 2.4, has been lumped at a MIDR of 6.0% for clarity, with the number of records causing collapse indicated in parentheses. Due to the relatively severe design intensity specified by the EC8 response spectrum, at all sites, the structural response approaches the design drift limit of 2.0% at an intensity level with a much lower annual exceedance rate than that of 1/475 assigned to the design spectrum. As a consequence, the most influential data anchoring the life safety limit state fragility function is associated with ground motions with relatively low exceedance rates and therefore the potential inconsistency with the hazard scenarios produced by the exceedance disaggregation is likely mitigated.
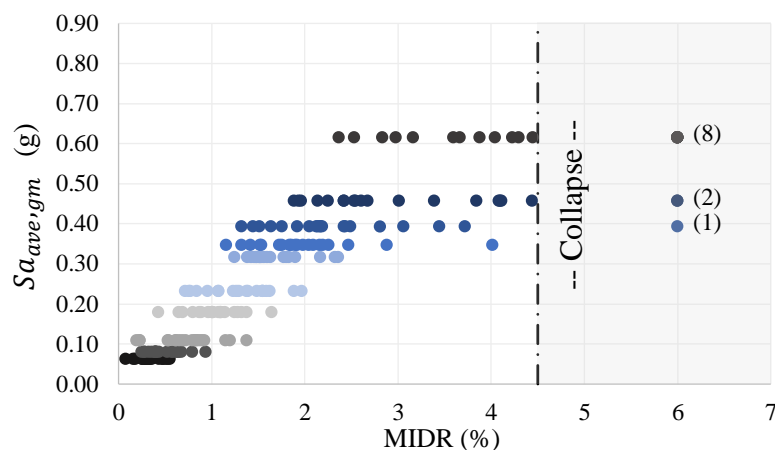
Figure 4.1 Athens MSA results
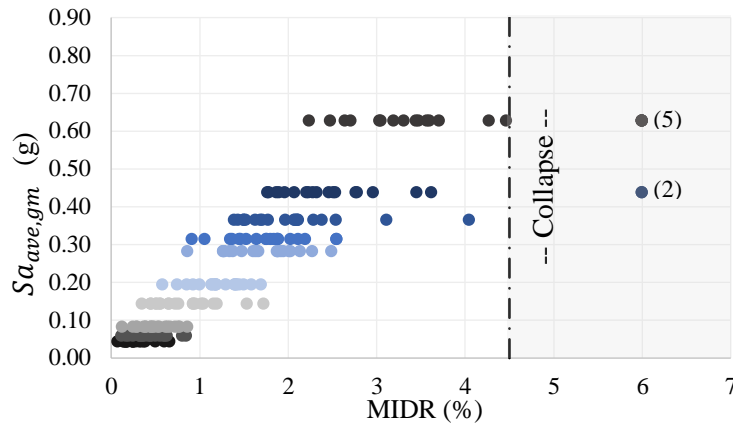
Figure 4.2 Perugia MSA results
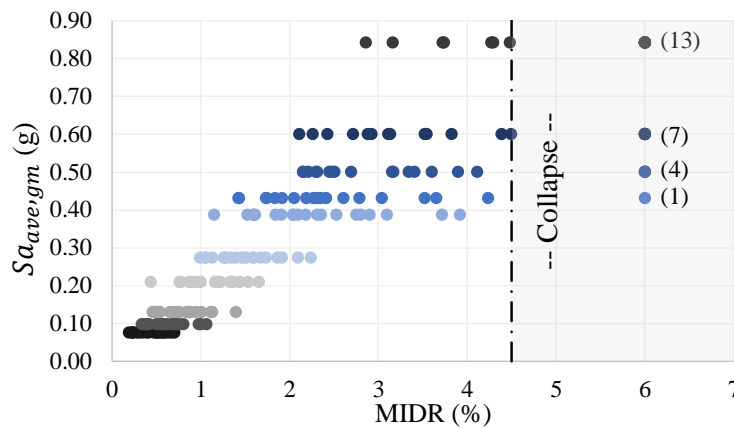
Figure 4.3 Focsani MSA results

4.2 Response Uncertainty

In the framework of probabilistic risk assessment, it is essential to account for both aleatory and epistemic sources of uncertainty that influence the predictability of structural response caused by earthquake-induced ground motions. Uncertainty in the building's response due to the aleatory sources represents the randomness in the earthquake ground motions that are observed in nature and is denoted as the record-to-record variability (RTR var.). The record-to-record variability is inherently captured by the distributions evaluated from the structural response simulations of the MSA for each suite of ground motions with a known intensity level, $IM = x$. That is, the record-to-record variability reflects the uncertainty in the random variable of MIDR, remaining when only the IM of Sa_{ave} is used for prediction. The aleatory uncertainty for a given number of analyses can be reduced by conditioning the response on an IM with higher efficiency or, alternatively, by performing more response analyses. Epistemic uncertainty, however, is introduced when the stochastic nature of reality is somewhat simplified to facilitate the building response to be simulated for a given input ground motion. Namely, random variables such as component strength, stiffness, and deformation capacity are treated as deterministic parameters when modelling the building. Epistemic uncertainty is essentially due to the lack of knowledge about the phenomena being modelled and, therefore, can be reduced by acquiring more information through testing.

Previous research, primarily focused on the pre-collapse response of structures, has indicated that modelling uncertainties associated with damping, mass and material strengths have a

relatively small effect on the overall uncertainty in seismic performance predictions. [Porter *et al.*, 2002; Lee and Mosalam, 2005]. Whereas accounting for uncertainty in the definition of element model parameters for post-peak and softening response can have a significant influence on the estimated performance, particularly for collapse risk analysis. [Ibarra and Krawinkler, 2005]. Several methods can be used to propagate modelling uncertainties to account for their effect in probabilistic risk assessment; however, the accuracy, computational effort and complexity can vary significantly [Liel *et al.*, 2009]. For example, the effect of modelling uncertainties can be assessed using a response surface defined by correlated random variables which can be utilised to simulate the structural response with methods such as Monte Carlo simulation or Latin hypercube sampling. Although such methods provide superior accuracy with an ability to predict the effect of modelling uncertainty on both the median capacity and dispersion, they are computationally expensive. For this reason, the simpler yet inferior alternative of the first-order second-moment method (FOSM) is often adopted as a more practical option in practice. However, the FOSM method lacks the ability to predict a shift in the median capacity, as will be seen below.

4.3 Fragility Analysis

Using the MSA results shown in Figures 4.1 to 4.3, a set of fragility functions were produced for each site to define the probability of the random variable of MIDR exceeding a range of response limits z_i, given the occurrence of a ground motion with intensity $Sa_{ave} = x$. The two key fragility functions of interest corresponding to the design limit state capacity of 2.0% and the collapse limit state capacity of 4.5% are shown in Figures 4.4 to 4.6 for the three sites in Athens, Perugia and Focsani, respectively. In this study, the FOSM method is used to combine both the record-to-record variability and modelling variability into a single aggregate value to propagate their combined effect in the risk assessment. It has been assumed that the structural model used for the response estimation is unbiased and a $\beta_{U,MIDR|IM,C'}$ value of 0.25 is a fair representation of the logarithmic standard deviation in the response due to sources of epistemic uncertainty. However, in the computation of the collapse fragility function, a value of $\beta_{U,C|IM} = 0.3$ has been assumed. It can be seen from the comparisons shown in Figures 4.4 to 4.6 that in the presence of modelling uncertainty, the probability of exceeding the defining limit state capacity increases for intensities less than the median capacity but decreases for intensities higher than the median. As a consequence, when convolving the fragility functions with the hazard, ground motions with a lower intensity but higher rate of occurrence contribute more to the risk of exceeding the limit state capacity.

Another consequence of the relatively low hazard at the three sites compared to the design intensity can be seen by the analytical data used to anchor the collapse fragility functions. Although the MSA was performed with ground motion suites up to an intensity level with a return period of 25 thousand years, only the hazard at the Focsani site was capable of producing collapse data above the median capacity. One could supplement the existing MSA results with additional stripes at more severe intensities to provide more robust estimates of the collapse fragility curves. However, given that the probability of exceeding the highest intensity level is 0.2% in 50 years, it is likely that supplementing the existing data will be futile as stripes capable of producing data above the median have an occurrence rate that has negligible influence on the collapse risk.
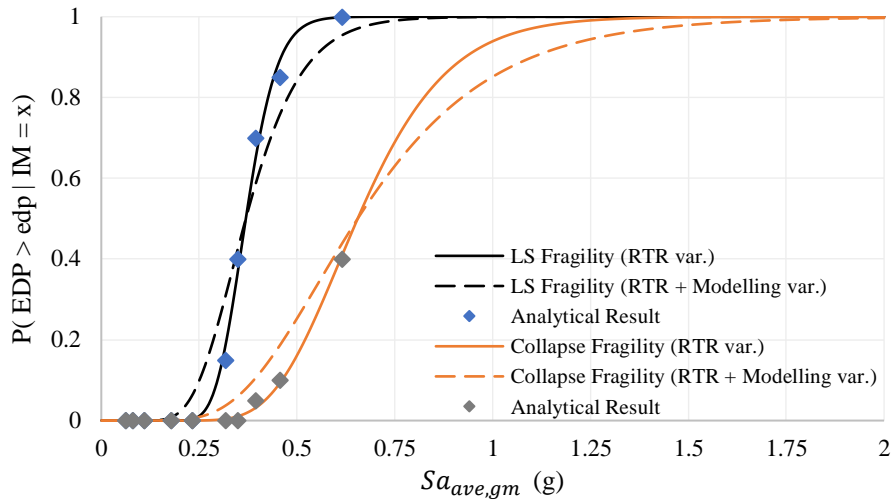
Figure 4.4 Athens fragility functions
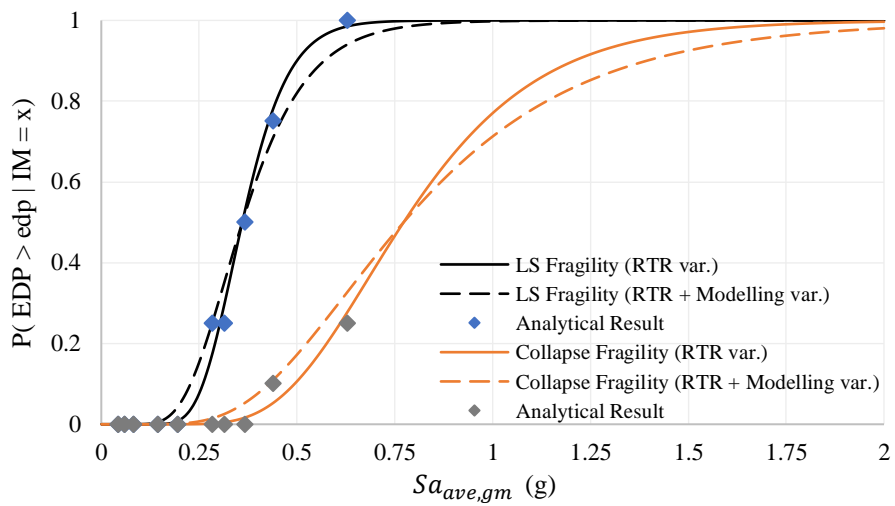
Figure 4.5 Perugia fragility functions
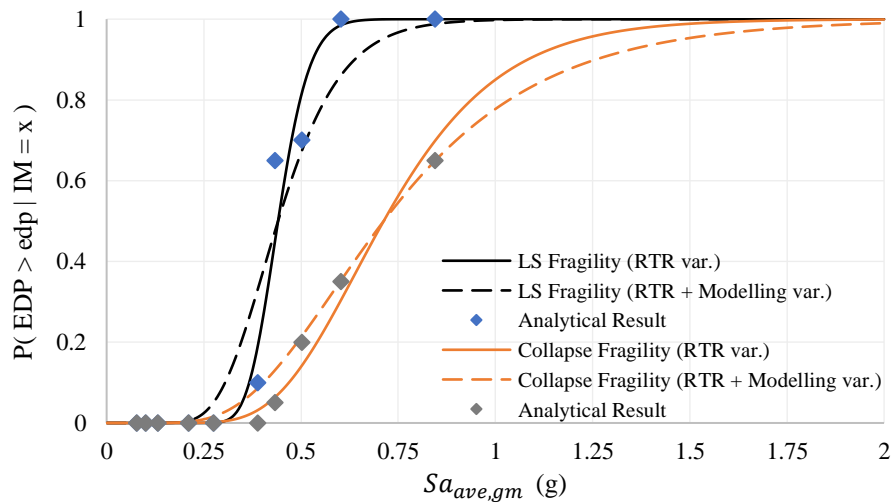
Figure 4.6 Focsani fragility functions

A direct comparison between the LS fragility and collapse fragility functions for the three sites are presented in Figures 4.7 and 4.8, respectively, with the estimated fragility function parameters summarised in Figure 4.9. As shown in Figure 4.7, the capacity of the life safety limit state targeted in the DDBD procedure is site-dependent with a median capacity ranging between 0.36 g $< Sa_{ave} < 0.44$ g. To put in perspective the degree of variation between the LS median capacities due to the variation in the hazard characteristics, the return periods of the respective intensities have been quantified by evaluating the site-specific hazard curves shown in Figure 3.3. It was found that the variation indicated by Figure 4.7 corresponds to a median capacity with a return period ranging between approximately 3400 – 4700 years. Furthermore, no pattern can be observed by comparing the LS capacity curves to the collapse capacity curves. For example, the site in Perugia produces the lowest LS capacity but the highest collapse capacity, and therefore the collapse performance cannot be implied from the LS performance.
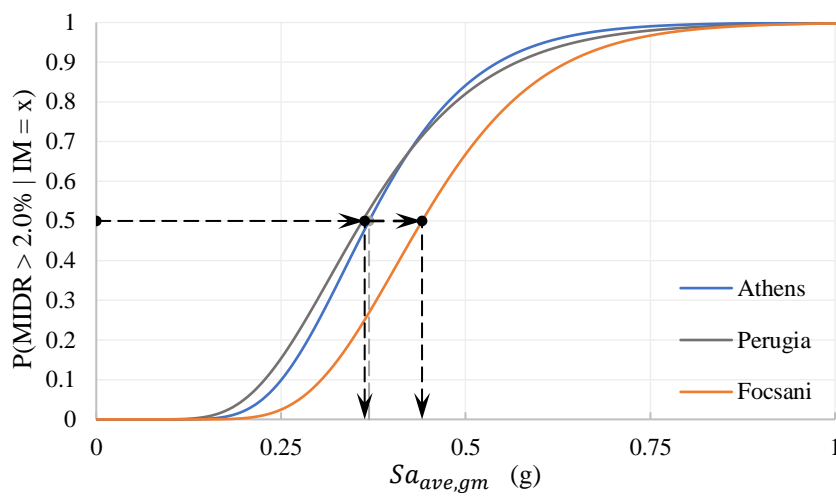
Figure 4.7 Design limit state fragility comparison
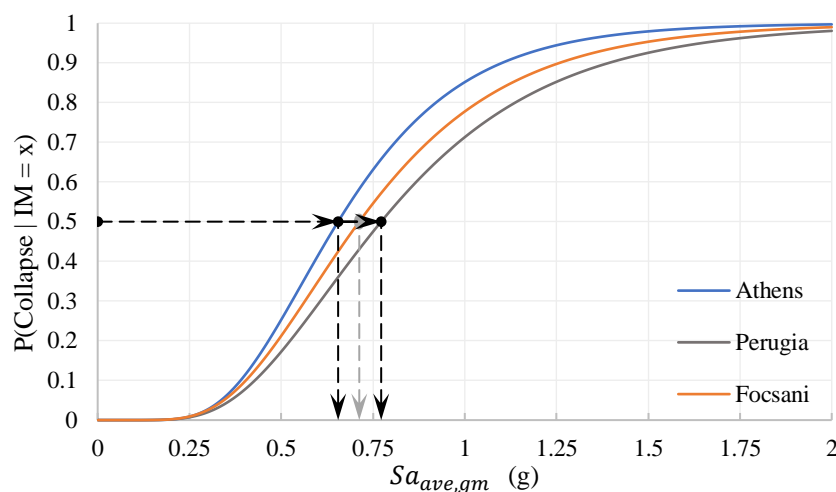
Figure 4.8 Collapse fragility comparison
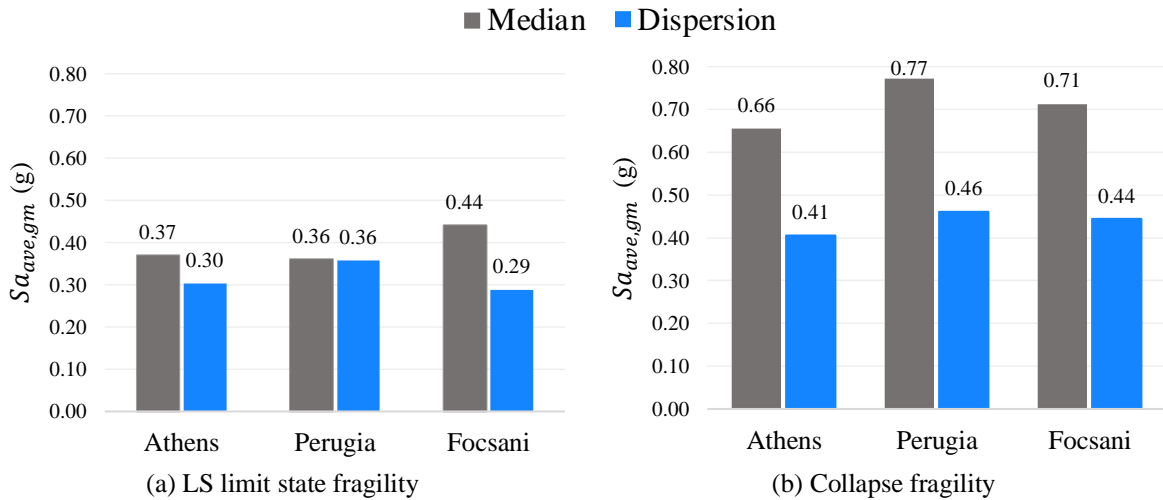
Figure 4.9 Comparisons of fragility curve parameters

4.3 MIDR Hazard

For each fragility function covering the range of response limits z_i, Equation 3.6 was used to combine the probability of exceeding each MIDR response, due to a ground motion with intensity Sa_{ave}, with the likelihood of Sa_{ave} occurring. The resulting locus of points produces the site-dependent MIDR hazard curve defining the mean annual frequency of exceedance of MIDR $> z_i$. This process was repeated with the set of seismic hazard curves scaled to be consistent with the design intensity as discussed in Section 3.4.1 in an attempt to isolate the variation in building performance attributed to the DDBD procedure. Figure 4.10 compares the MIDR hazard curves for the same building as a result of the scaled and unscaled hazard at the sites located in Athens, Perugia and Focsani.
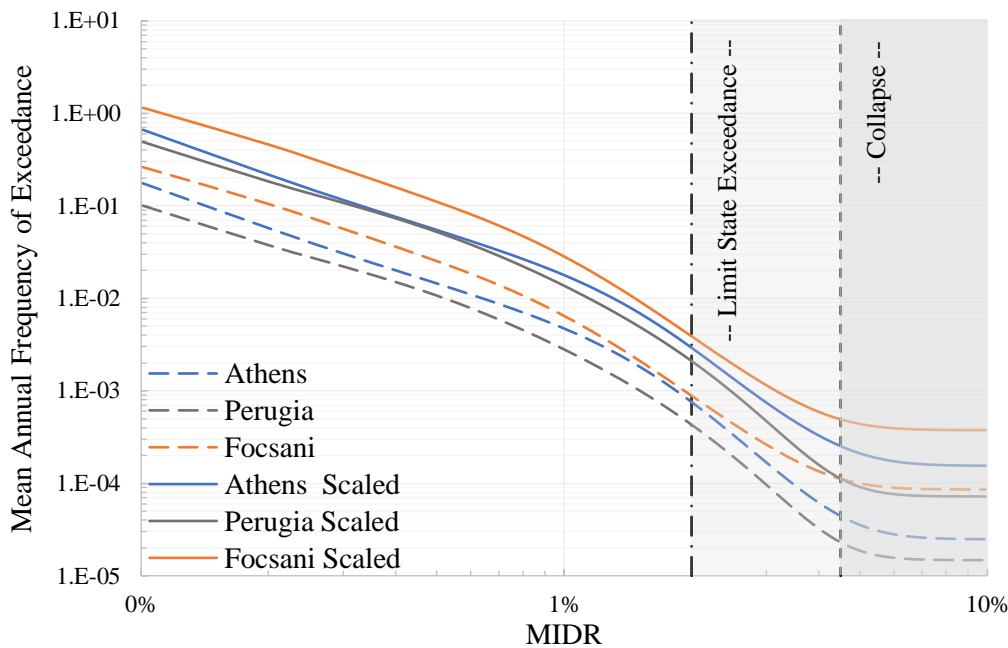
Figure 4.10 MIDR hazard comparison

45

The building performance is quantified by evaluating the site-specific MIDR hazard curve at the limit state capacity of 2.0% targeted by the DDBD method to determine the mean annual frequency of the performance objective not being met. By making the common assumption that the Poisson distribution can adequately represent the time-dependent occurrence of earthquake events, the numerical values of the MAF are expressed in terms of the probability of exceedance in 50 years (PoE/50) to aid in the interpretation of results. Hence, the transformation between the MAF determined from Figure 4.10 to PoE/50 is given by Equation 4.1 with the performance evaluation is presented in Figure 4.11.

$$PoE/50 = (1-e^{-MAF \cdot 50}) \cdot 100\% \qquad (4.1)$$

As discussed in Section 3.4.1, two variables influence the risk of the building response violating the performance objective. Namely, the effect of hazard inconsistency with the EC8 design spectrum and the effect that the DDBD method has on the building performance. It can be seen by comparing the building performance at the three sites that the risk of exceeding the performance objective is relatively low with an average PoE/50 of 3.4%. However, the performance is obviously dominated by the effect of hazard inconsistency, with the design spectrum severely overestimating the demand, as shown by the UHS comparisons in Figure 3.1. Despite the reasonably mundane demand at the three sites compared with the design intensity, a variation in the performance of over 200% is observed; although only a portion of this total variation can be attributed to the effectiveness of the DDBD method.

(a) MAF of exceeding 2.0% MIDR   (b) Probability of MIDR > 2.0% in 50 years
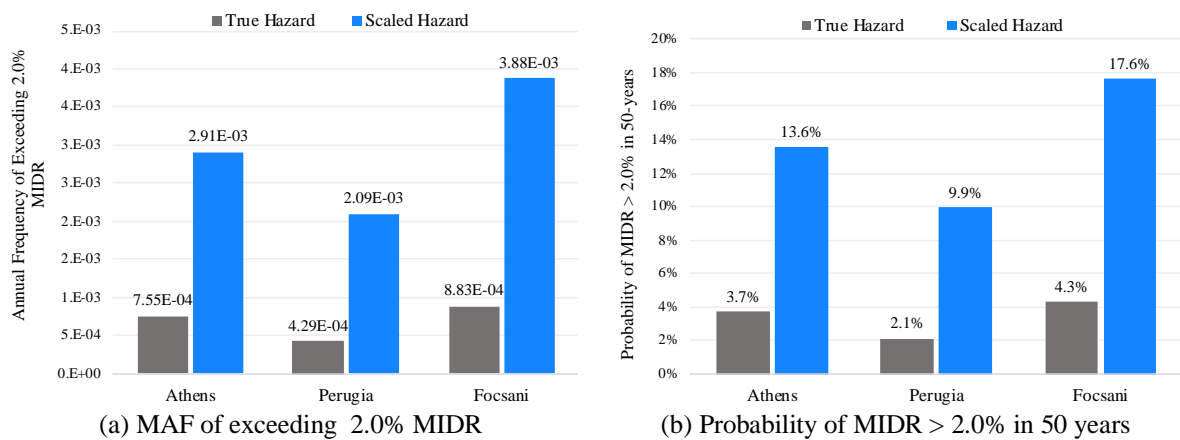
Figure 4.11 Limit state risk performance

After repeating the risk analysis with the set of hazard curves consistent with the EC8 design spectrum, the performance attributed to the effectiveness of the DDBD method is revealed. It can be seen that the variation in the MAF of exceeding the limit state capacity reduced by less than 15%, producing a performance range of approximately 1.0 – 1.8 times the MAF of the design intensity.

Although not explicitly considered in the design of the building, the performance assessment is extended to the collapse limit state by evaluating the MIDR hazard curve at the estimated collapse capacity of 4.5%. A significant variation of almost 500% is observed in the collapse risk between the three sites, with a probability of collapse in 50 years ranging between 0.11% − 0.56%. Again, after repeating the risk assessment with the set of the hazard curves consistent with the EC8 design spectrum, only a small reduction in the performance variation of 10% is observed, with the probability of collapse in 50 years ranging between 0.6 − 2.4%.

(a) MAF of Collapse　　　　　　　　(b) Probability of collapse in 50 years
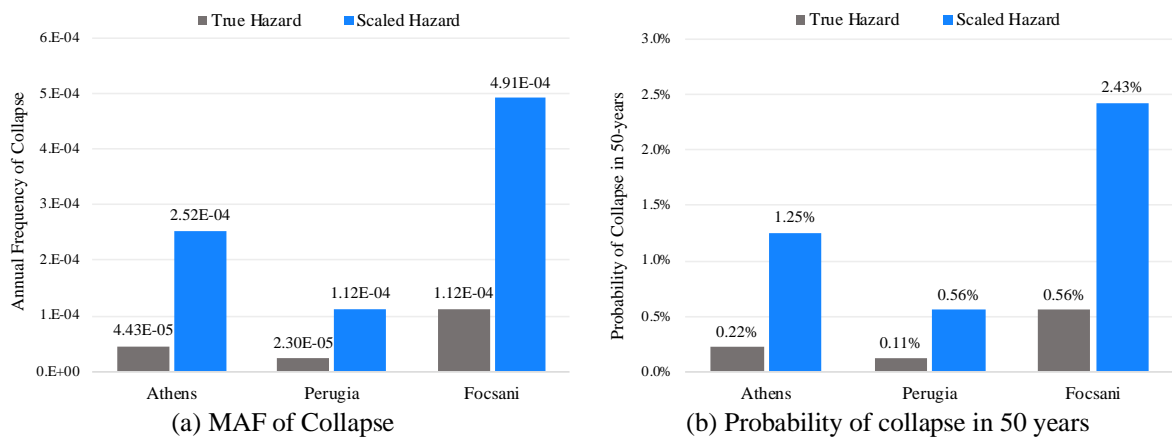
Figure 4.12 Collapse risk performance

The observed variation in the building's performance indicates, once more, that checking the probability of exceedance of the design intensity level reveals little about the probability of exceedance of the target response. This observation emphasises the significance of accounting for sources of uncertainty that are inherent in the random structural capacity and the random structural demand due to earthquake-induced ground motions. Acknowledgement of the sources of uncertainty that dilute the predictability of the structural response shows that the exceedance of the limit state performance can occur due to hazard levels other than that considered by the DDBD method. Furthermore, as a consequence of the different hazard characteristics in the vicinity of the influential intensity levels, the amplification in the response MAF is highly site-dependent.

5 CONCLUSIONS

This thesis has investigated the ability of the innovative design procedure known as Direct Displacement-Based Design to produce structures with a uniform risk of exceeding a target performance objective. The study considered a single, completely regular, four-storey reinforced concrete wall building, designed according to the current Eurocode provisions to be suitable for three high seismicity sites located in Athens, Perugia and Focsani. Probability theory was used to fully characterise the maximum inter-storey drift ratio risk at the three sites by employing the PEER Performance-Based Earthquake Engineering methodology. The seismic hazard was linked to the structural response by performing a probabilistic seismic hazard analysis for the conditioning ground motion intensity measure of Sa_{ave}. Hazard disaggregation was performed at ten intensity levels to facilitate the selection of 200 hazard consistent ground motions using the exact CS method to represent the conditional mean and dispersion of spectral acceleration for each site covering the ten intensity levels considered. The multiple stripes analysis procedure was then used to collect analytical data to estimate the probability of exceeding a given structural response defined by the random variable of MIDR, due to a ground motion with intensity Sa_{ave}. The first-order second-moment method was used to combine both the record-to-record variability and modelling uncertainty into a single aggregate value to propagate the combined effect in the risk assessment. The building fragility functions were convolved with the seismic hazard to produce site-dependent MIDR hazard curves defining the mean annual frequency of exceeding a specified MIDR threshold.

The performance of the DDBD method in terms of its ability to alleviate the computational burden of PBSD methods was investigated by evaluating the variability in the risk of the performance objective not being met. It was found that the variation in the MAF of exceeding the LS limit state capacity attributed to the effectiveness of the DDBD method was approximately $1.0 – 1.8$ times the MAF of the design intensity. Furthermore, although not explicitly considered in the building design, the risk assessment was extended to the collapse limit state, which revealed a variation in the mean annual frequency of collapse of over 400%. Therefore, based on the assessment of only a single building, the results indicate that the DDBD method at best provides designs that satisfy damage control criteria through controlling drift at a specified level of seismic intensity but with widely varying risk levels. Consequently, the results indicate that the simple deterministic alternative of DDBD lacks the ability to bridge the gap between current structural design and the computationally demanding probabilistic methods embraced by pure PBEE.

The scope of this thesis will be extended with future research to include different building typologies and dynamic characteristics to better characterise the variation in risk with the ultimate goal of moving DDBD closer to PBSD.

REFERENCES

Baker, Jack & Allin Cornell, C. (2005). Vector-valued ground motion intensity measure consisting of spectral acceleration and epsilon. Earthquake Engineering & Structural Dynamics. 34. 1193 - 1217. 10.1002/eqe.474.

Baker, Jack & Allin Cornell, C. (2006a). Spectral shape, epsilon and record selection. Earthquake Engineering & Structural Dynamics. 35. 1077 - 1095. 10.1002/eqe.571.

Baker, Jack & Allin Cornell, C. (2006b). Which Spectral Acceleration Are You Using?. Earthquake Spectra - EARTHQ SPECTRA. 22. 10.1193/1.2191540.

Baker, Jack & Allin Cornell, C. (2008). Vector-valued intensity measures for pulse-like near-fault ground motions. Engineering Structures. 30. 1048-1057. 10.1016/j.engstruct.2007.07.009.

Baker, Jack & Jayaram, Nirmal. (2008). Correlation of Spectral Acceleration Values from NGA Ground Motion Models. Earthquake Spectra - EARTHQ SPECTRA. 24. 10.1193/1.2857544. [Baker and Jayaram, 2008)

CEN, (EN1992 – 1: 2004). Eurocode 2: Design of concrete structures -Part 1: General rules and rules for buildings, Brussels: European Committee for Standardization

CEN, (EN1998 – 1: 2004). Eurocode 8: Design of Structures for Earthquake Resistance -Part 1: General Rules, Seismic Actions and Rules for Buildings, Brussels: European Committee for Standardization

Jack W. Baker (2015) Efficient Analytical Fragility Function Fitting Using Dynamic Structural Analysis. Earthquake Spectra: February 2015, Vol. 31, No. 1, pp. 579-599.

Bazzurro, Paolo & A Cornell, C. (1999). Disaggregation of Seismic Hazard. Bulletin of the Seismological Society of America. 89.

Bazzurro, Paolo & A. Cornell, C. (2002). Vector-valued probabilistic seismic hazard analysis (VPSHA). Seismological Research Letters. 72.

M. Boore, David & Atkinson, Gail. (2008). Ground-Motion Prediction Equations for the Average Horizontal Component of PGA, PGV, and 5%Damped PSA at Spectral Periods between 0.01 s and 10.0 s. Earthquake Spectra - EARTHQ SPECTRA. 24. 10.1193/1.2830434.

Bradley, Brendon. (2010). A generalized conditional intensity measure approach and holistic ground-motion selection. Earthquake Engineering & Structural Dynamics. 39. 1321 - 1342. 10.1002/eqe.995.

Cornell, C.A. (1968): Engineering Seismic Risk Analysis, Bulletin of Seismological Society of America, Vol. 58, pp. 1583-1606.

REFERENCES

A. Cornell, C & Krawinkler, H. (2000). Progress and Challenges in Seismic Performance Assessment. PEER Center News. 3.

Allin Cornell, C & Jalayer, F & Hamburger, Ronald & A. Foutch, Douglas. (2002). Probabilistic Basis for 2000 SAC Federal Emergency Management Agency Steel Moment Frame Guidelines. Journal of Structural Engineering-asce - J STRUCT ENG-ASCE. 128. 10.1061/(ASCE)0733-9445(2002)128:4(526).

Deierlein, Gregory & Krawinkler, H & Cornell, C.A.. (2003). A framework for performance-based earthquake engineering. 1-8.

Eads, Laura & Miranda, Eduardo & Lignos, Dimitrios. (2015). Average spectral acceleration as an intensity measure for collapse risk assessment. Earthquake Engineering & Structural Dynamics. 44. 10.1002/eqe.2575.

European Facilities for Earthquake Hazard and Risk, EFEHR [2017], accessed September 2018: <http://www.efehr.org>

Faccioli, Ezio & Paolucci, Roberto & Rey, Julien. [2004]. Displacement Spectra for Long Periods. Earthquake Spectra - EARTHQ SPECTRA. 20. 10.1193/1.1707022.

Fox, Matt & Stafford, Peter & Sullivan, T. (2016). Seismic hazard disaggregation in performance-based earthquake engineering: Occurrence or exceedance? Earthquake Engineering & Structural Dynamics. 45. 835-842. 10.1002/eqe.2675.

A. Goulet, Christine & Haselton, B & Mitrani-Reiser, J & L. Beck, James & Deierlein, Gregory & Porter, Keith & Stewart, Jonathan. [2007]. Evaluation of the seismic performance of a code-conforming reinforced-concrete frame building - From seismic hazard to collapse safety and economic losses. Earthquake Engineering & Structural Dynamics - 1973-1997. 10.1002/eqe.694

Haselton, Curt & Baker, Jack. (2006). Ground motion intensity measures for collapse capacity prediction: Choice of optimal spectral period and effect of spectral shape.

Haselton, Curt & Baker, Jack & Liel, Abbie & Deierlein, Gregory. (2011). Accounting for Ground Motion Spectral Shape Characteristics in Structural Collapse Assessment Through an Adjustment for Epsilon. Journal of Structural Engineering. 137. 10.1061/(ASCE)ST.1943-541X.0000103.

F. Ibarra, Luis & advisor Krawinkler, Helmut. (2005). Global Collapse of Frame Structures Under Seismic Excitations.

Jalayer F. (2003). Direct probabilistic seismic analysis: implementing non-linear dynamic assessment, in Department of Civil and Environmental Engineering, Stanford University: Stanford, CA.

Kohrangi, Mohsen & Vamvatsikos, Dimitrios & Bazzurro, Paolo. (2016). Implications of IM selection for seismic Loss Assessment of 3D Buildings. Earthquake Spectra. 32. 10.1193/112215EQS177M.

Kohrangi, Mohsen & Vamvatsikos, Dimitrios. (2017). Site dependence and record selection schemes for building fragility and regional loss assessment. Earthquake Engineering & Structural Dynamics. 10.1002/eqe.2873.

Kohrangi, Mohsen & Bazzurro, Paolo & Vamvatsikos, Dimitrios & Spillatura, Andrea. (2017). Conditional spectrum-based ground motion record selection using average spectral acceleration. Earthquake Engineering & Structural Dynamics. 46. 10.1002/eqe.2876.

REFERENCES

Kohrangi, Mohsen & Bazzurro, Paolo & Vamvatsikos, Dimitrios (2018a) Conditional spectrum bi-directional record selection for risk assessment of 3D structures using scalar and vector IMs, Earthquake Engineering and Structural Dynamics (accepted).

Kohrangi, Mohsen & Vamvatsikos, Dimitrios & Bazzurro, Paolo. (2018b). Pulse-like versus non-pulse-like ground motion records: Spectral shape comparisons and record selection strategies. Earthquake Engineering & Structural Dynamics. 10.1002/eqe.3122.

Kohrangi, Mohsen (2019) Personal correspondence: Hazard and disaggregation computation for three sites located in Athens, Perugia and Focsani.

Lee, Tae-Hyung & Mosalam, Khalid. (2005). Seismic demand sensitivity of reinforced concrete shear-wall building using FOSM method. Earthquake Engineering & Structural Dynamics. 34. 1719 - 1736. 10.1002/eqe.506.

Liel, Abbie & Haselton, Curt & Deierlein, Gregory & Baker, Jack. (2009). Incorporating Modeling Uncertainties in the Assessment of Seismic Collapse Risk of Buildings. Structural Safety. 31. 197-211. 10.1016/j.strusafe.2008.06.002.

Lin, Ting & Harmsen, Stephen & Baker, Jack & Luco, Nicolas. (2013). Conditional Spectrum Computation Incorporating Multiple Causal Earthquakes and Ground-Motion Prediction Models. The Bulletin of the Seismological Society of America. 103. 1103-1116. 10.1785/0120110293.

Luco, Nicolas & Allin Cornell, C. (2007). Structure-Specific Scalar Intensity Measures for Near-Source and Ordinary Earthquake Ground Motions. Earthquake Spectra. 23. 10.1193/1.2723158.

Mander, J.B. & M. J. N., Priestley. (1988). Theoretical Stress-Strain Model for Confined Concrete. Journal of Structural Engineering. 114. 10.1061/(ASCE)0733-9445(1988)114:8(1804).

Monelli, Damiano & Pagani, Marco & Weatherill, Graeme & Silva, Vitor & Crowley, Helen. (2012). The hazard component of OpenQuake: The calculation engine of the Global Earthquake Model. 10.13140/2.1.3307.1364.

Pacific Earthquake Engineering Research Center (PEER). (2008). PEER Next Generation Attenuation (NGA) database. http://peer.berkeley .edu/nga/

Porter, Keith & L. Beck, James & V. Shaikhutdinov, Rustem. (2002). Sensitivity of Building Loss Estimates to Major Uncertain Variables. Earthquake Spectra. 18. 10.1193/1.1516201.

Priestley, M.J.N. (1993). Myths and Fallacies in Earthquake Engineering – Conflicts Between Design and Reality Bulletin of the NZ National Society for Earthquake Engineering, New Zealand, 26:3, 329-341.

Priestley, M. J. N., Calvi, G. M., and Kowalsky, M. J. [2017] Displacement-Based Seismic Design of Structures – 2nd Edition, Fondazione Eucentre, Pavia, Italy.

SeismoStruct (2018) SeismoStruct—software: a computer program for static and dynamic nonlinear inelastic analysis of structures < https://www.seismosoft.com>

Shibata, A & Sozen, Mete. [1976]. Substitute Structure Method for Seismic Design in Reinforced Concrete. Journal of the Structural Division. 102.

REFERENCES

Sullivan, T & Calvi, G & J. N. Priestley, M & Kowalsky, Mervyn. (2003). The limitations and performances of different displacement based design methods. Journal of Earthquake Engineering - J EARTHQU ENG. 7. 201-241. 10.1080/13632460309350478

Sullivan, T.J. Priestley, M.J.N., and Calvi, G.M., Editors (2012). A Model Code for the Displacement-Based Seismic Design of Structures, DBD12, IUSS Press, Pavia, Italy.

Vamvatsikos, Dimitrios & Allin Cornell, C. (2002). Incremental Dynamic Analysis. Earthquake Engineering & Structural Dynamics. 31. 491 - 514. 10.1002/eqe.141.

Vamvatsikos, Dimitrios & Aschheim, Mark. (2016). Performance-based seismic design via yield frequency spectra ‡. Earthquake Engineering & Structural Dynamics. n/a-n/a. 10.1002/eqe.2727.

Zareian, Farzin & Krawinkler, Helmut. (2007). Assessment of probability and design for collapse safety. Earthquake Engineering & Structural Dynamics. 36. 1901 - 1914. 10.1002/eqe.702.

APPENDIX A – Selected Records for Response Assessment

Table A.1: Selected Records for Athens

Record	IM1 Seq #	IM1 X/Y	IM1 SF	IM2 Seq #	IM2 X/Y	IM2 SF	IM3 Seq #	IM3 X/Y	IM3 SF	IM4 Seq #	IM4 X/Y	IM4 SF	IM5 Seq #	IM5 X/Y	IM5 SF
1	1779	X	2.01	1779	X	2.56	1803	Y	2.87	2492	X	2.96	3295	X	4.08
2	541	Y	6.97	437	X	5.38	437	Y	7.15	879	Y	0.57	773	X	3.33
3	897	X	2.52	497	Y	3.06	550	X	1.98	3512	Y	1.64	2655	Y	1.63
4	2492	X	1.07	2716	Y	3.11	2460	Y	2.37	1544	Y	1.81	522	X	3.22
5	2737	Y	2.21	1170	X	2.33	88	X	1.69	138	X	1.63	164	Y	1.91
6	836	X	0.84	1616	X	2.54	1616	X	3.37	1616	X	5.50	573	Y	1.12
7	297	Y	0.71	861	Y	0.92	1560	Y	1.72	3298	X	3.91	2112	Y	5.98
8	2003	Y	2.33	1315	X	1.93	3225	Y	7.28	1301	Y	3.78	1170	X	6.57
9	1819	Y	1.92	801	Y	0.67	1819	X	3.25	354	X	3.06	3296	Y	5.42
10	2874	Y	4.95	2591	Y	5.04	3440	Y	6.83	2986	Y	5.75	1348	X	5.08
11	572	Y	0.75	2618	X	0.48	739	X	0.81	2940	Y	6.19	1613	Y	6.65
12	997	Y	1.07	167	X	1.35	591	X	4.69	957	X	3.16	1616	Y	7.15
13	1092	Y	0.71	1358	X	1.15	1249	X	3.54	1229	X	2.27	1824	Y	6.34
14	971	Y	1.06	971	Y	1.34	971	Y	1.79	458	X	1.46	800	X	2.47
15	443	Y	6.97	743	X	1.39	993	Y	1.09	993	X	1.78	2994	Y	5.28
16	2004	X	6.26	1172	X	3.18	719	Y	1.22	1153	X	2.47	673	X	5.71
17	2855	X	5.23	1611	X	0.89	1611	X	1.18	870	Y	2.39	1505	X	0.35
18	1518	Y	1.43	1000	X	0.93	1518	X	2.42	1518	X	3.95	984	X	2.69
19	618	X	1.94	548	X	0.76	754	Y	0.92	1024	X	2.12	1113	X	2.04
20	3207	Y	1.60	3207	X	2.04	529	X	0.44	2375	Y	8.33	329	X	5.66

APPENDIX A – Selected Records for Response Assessment

Record	IM6			IM7			IM8			IM9			IM10		
	Seq #	X/Y	SF	Seq #	X/Y	SF	Seq #	X/Y	SF	Seq #	X/Y	SF	Seq #	X/Y	SF
1	3549	X	6.80	2623	X	8.95	3091	Y	9.65	3407	X	9.06	1398	Y	9.15
2	2648	X	6.48	849	Y	4.02	801	Y	3.20	408	X	4.76	408	Y	6.41
3	393	Y	7.60	1611	X	3.75	1161	Y	2.64	1161	X	3.07	2744	Y	7.19
4	1837	X	9.19	3320	X	5.63	1259	X	6.34	1259	Y	7.36	1211	X	7.20
5	1000	Y	3.57	1509	X	0.77	3504	X	4.30	1202	Y	1.69	3509	X	7.59
6	2744	Y	3.70	1279	Y	4.89	1278	X	3.44	1439	Y	8.79	1267	X	6.52
7	1475	Y	2.39	294	X	7.33	1518	Y	8.70	1811	Y	9.27	2651	Y	9.74
8	2710	X	3.29	2710	Y	3.60	2710	Y	4.08	3500	Y	7.02	1490	Y	3.25
9	2723	X	8.67	1541	X	1.34	1505	X	0.60	1611	X	4.93	883	Y	8.71
10	1452	X	7.62	1499	Y	2.25	900	Y	1.82	1434	X	4.28	1116	X	3.03
11	185	Y	1.30	1478	X	1.70	737	Y	2.53	180	Y	1.08	2464	Y	9.96
12	3488	Y	9.04	1202	Y	1.29	1839	Y	8.41	789	X	5.25	789	X	7.08
13	1043	X	3.79	1243	X	3.38	2500	Y	5.94	1500	Y	2.11	173	X	2.49
14	1233	Y	3.17	180	X	0.82	1196	Y	5.65	800	Y	4.86	877	X	9.93
15	2973	Y	6.92	2501	X	5.41	3500	Y	6.04	2704	Y	5.60	2501	Y	9.59
16	233	Y	4.92	233	Y	5.39	150	Y	2.42	150	X	2.82	150	X	3.80
17	2510	Y	4.47	1523	Y	2.70	1330	X	3.99	896	X	6.34	1542	X	2.34
18	1083	X	2.77	728	Y	1.62	1094	X	7.85	1094	Y	9.13	2893	X	8.27
19	1839	X	6.78	1503	X	0.51	1503	X	0.58	1503	Y	0.68	2114	X	1.24
20	743	Y	5.35	794	Y	5.08	794	X	5.74	794	Y	6.67	1083	X	5.39

Ground motion sequence number from NGA database (Seq #), Selected component for response analysis (X/Y), Scale Factor (SF)

Table A.2: Selected Records for Perugia

Record	IM1			IM2			IM3			IM4			IM5		
	Seq #	X/Y	SF	Seq #	X/Y	SF	Seq #	X/Y	SF	Seq #	X/Y	SF	Seq #	X/Y	SF
1	2478	Y	0.89	2478	Y	1.19	2460	X	1.77	2648	X	2.94	2839	X	9.99
2	3176	Y	2.13	541	X	6.29	541	Y	8.81	3209	Y	4.24	3207	Y	4.82
3	1935	X	7.52	2703	Y	0.81	436	Y	5.54	897	X	5.59	1107	X	0.97
4	1170	Y	1.23	172	Y	0.72	1620	Y	5.36	1615	Y	1.80	946	Y	7.69
5	1577	Y	1.92	1053	Y	0.96	2946	Y	1.99	947	X	2.23	77	Y	0.41
6	762	X	0.58	520	Y	4.10	535	X	3.01	1338	Y	3.10	3458	Y	4.54
7	3437	X	3.63	3381	Y	2.27	1436	Y	0.69	1042	X	0.69	183	X	0.62
8	454	Y	2.31	167	X	0.96	288	Y	1.02	1148	Y	1.52	802	X	0.69
9	545	Y	2.25	698	X	2.35	996	X	0.69	1821	Y	3.50	832	X	1.29
10	2874	Y	3.32	720	X	0.52	325	Y	2.63	1313	Y	2.74	828	Y	0.48
11	320	X	0.55	712	Y	1.67	992	X	1.10	1842	X	5.36	1118	X	1.33
12	552	Y	1.52	552	X	2.05	616	X	1.22	1053	X	2.36	466	Y	2.90
13	1511	Y	0.13	728	Y	0.27	1108	Y	0.26	982	X	0.25	2867	X	7.94
14	2259	X	3.79	3205	X	2.08	817	Y	5.80	3302	Y	1.57	800	X	2.07
15	1051	Y	0.12	125	Y	0.46	125	Y	0.65	3480	X	3.00	3501	X	3.77
16	2772	X	7.99	2697	X	3.39	981	X	1.10	710	Y	4.55	673	X	4.79
17	1763	X	2.03	1763	X	2.73	3455	Y	2.15	832	Y	0.95	2472	Y	2.78
18	747	Y	2.01	747	X	2.71	1518	X	1.81	730	Y	1.24	562	Y	3.06
19	3211	Y	0.85	16	Y	1.52	968	X	0.88	2654	X	1.61	2654	Y	2.18
20	619	Y	0.44	819	X	3.48	633	X	1.54	1003	X	0.78	2626	X	2.55

APPENDIX A – Selected Records for Response Assessment

Record	IM6 Seq #	IM6 X/Y	IM6 SF	IM7 Seq #	IM7 X/Y	IM7 SF	IM8 Seq #	IM8 X/Y	IM8 SF	IM9 Seq #	IM9 X/Y	IM9 SF	IM10 Seq #	IM10 X/Y	IM10 SF
1	3086	Y	6.58	3086	Y	7.33	514	X	5.05	514	X	6.04	189	X	3.78
2	3512	X	2.58	247	X	8.02	3080	Y	4.73	324	X	5.09	1492	Y	0.88
3	993	Y	2.82	212	Y	3.46	393	X	8.77	849	Y	5.07	978	Y	4.12
4	1005	X	2.86	1118	Y	2.15	1838	X	9.77	961	X	9.37	3024	Y	9.40
5	1042	Y	1.35	1119	X	0.59	2709	Y	4.13	1202	Y	1.62	838	X	5.32
6	783	X	1.05	1155	Y	2.34	3496	Y	3.39	182	Y	1.01	756	X	6.42
7	2112	X	7.27	1377	Y	7.56	170	X	1.27	3265	X	3.34	878	X	5.86
8	1148	Y	2.98	2948	Y	8.31	1637	X	3.42	3317	Y	2.21	3500	Y	9.64
9	1181	Y	2.79	1503	Y	0.46	1505	X	0.56	2706	X	7.60	1316	X	4.66
10	1059	X	4.10	953	Y	0.78	1282	X	2.91	1221	X	3.92	1221	Y	5.62
11	1619	Y	4.96	1619	X	5.53	1209	Y	1.96	737	Y	2.81	292	X	1.89
12	2618	Y	1.66	1346	X	5.34	366	X	6.40	323	Y	9.20	341	Y	4.54
13	3515	X	8.10	3246	X	9.94	2971	Y	9.76	756	Y	4.48	1092	X	6.84
14	138	X	2.57	838	X	2.67	1277	Y	2.94	871	X	9.38	1541	Y	2.41
15	2973	X	6.16	2964	Y	7.75	266	X	2.40	138	X	3.98	1043	Y	7.51
16	612	X	9.85	637	X	5.66	637	X	6.58	150	Y	2.70	829	Y	2.99
17	861	Y	3.17	1204	X	1.86	1215	X	4.26	1472	Y	2.68	2884	Y	6.73
18	981	Y	3.81	1348	X	6.88	929	X	7.93	1083	X	3.83	862	X	5.62
19	884	Y	2.36	2723	X	8.60	1503	X	0.54	3322	X	9.34	1470	Y	6.14
20	753	Y	1.06	329	X	7.66	1283	Y	4.67	799	Y	2.77	1106	X	1.21

Ground motion sequence number from NGA database (Seq #), Selected component for response analysis (X/Y), Scale Factor (SF)

Table A.3: Selected Records for Focsani

	IM1			IM2			IM3			IM4			IM5		
Record	Seq #	X/Y	SF	Seq #	X/Y	SF	Seq #	X/Y	SF	Seq #	X/Y	SF	Seq #	X/Y	SF
1	2492	Y	1.27	3078	X	3.32	3413	Y	4.06	2452	X	2.67	1410	X	1.23
2	1622	X	3.99	3179	X	5.31	80	X	2.93	2950	Y	4.83	887	Y	9.79
3	497	Y	2.85	2005	Y	4.68	1633	Y	0.37	860	X	4.53	647	X	7.91
4	1170	Y	2.17	3108	Y	6.79	520	Y	9.25	1836	Y	6.76	2950	Y	6.29
5	1782	Y	1.85	747	X	4.60	535	Y	4.84	85	X	8.11	9	Y	6.58
6	836	Y	1.00	2697	X	5.77	807	Y	2.21	2654	Y	2.35	1489	Y	1.20
7	3385	Y	2.91	882	X	0.76	1764	Y	5.34	1214	X	4.53	981	X	3.70
8	1524	X	0.38	3513	Y	2.10	176	X	1.36	178	Y	0.97	1169	X	9.58
9	2725	Y	6.72	51	Y	3.25	1613	X	3.77	2704	Y	2.57	1551	X	1.03
10	3264	X	0.60	165	Y	0.52	1293	X	2.26	1348	Y	4.60	1509	Y	0.61
11	684	Y	4.25	1786	X	2.21	143	Y	0.21	93	X	3.43	1619	X	4.82
12	72	X	1.99	466	Y	1.48	766	X	0.52	323	X	4.42	1827	Y	4.46
13	2891	X	2.51	76	Y	9.67	1824	Y	3.60	392	X	4.34	721	X	1.03
14	1032	X	1.16	3302	X	1.09	3302	X	1.44	800	Y	2.23	2964	X	6.76
15	1303	X	1.26	981	X	1.34	2953	Y	3.70	2960	X	4.74	1272	X	6.62
16	1837	Y	2.22	1748	X	2.10	1670	X	2.61	1646	Y	2.92	612	X	9.57
17	2855	Y	6.19	1193	Y	0.34	2706	X	2.29	892	Y	3.87	2510	Y	3.87
18	1518	X	1.69	77	X	0.21	633	X	2.47	1512	Y	0.86	932	Y	7.77
19	95	Y	0.36	1833	Y	5.90	1801	Y	4.78	1505	X	0.32	1503	Y	0.41
20	633	X	1.44	125	X	0.78	2980	X	3.57	753	X	0.79	3364	X	6.84

APPENDIX A – Selected Records for Response Assessment

Record	IM6 Seq #	IM6 X/Y	IM6 SF	IM7 Seq #	IM7 X/Y	IM7 SF	IM8 Seq #	IM8 X/Y	IM8 SF	IM9 Seq #	IM9 X/Y	IM9 SF	IM10 Seq #	IM10 X/Y	IM10 SF
1	585	Y	1.25	585	Y	1.40	1364	Y	7.22	1373	Y	7.90	1078	X	6.19
2	1329	Y	2.75	1556	X	9.45	3472	X	8.00	3472	X	9.60	1415	Y	4.78
3	3312	X	7.08	178	X	2.00	2113	Y	9.23	2719	Y	9.92	1329	X	5.99
4	322	Y	2.31	1293	X	7.41	986	X	3.27	960	Y	1.98	1634	X	3.99
5	746	X	5.55	749	X	9.29	1202	Y	1.86	1202	X	2.23	849	Y	9.77
6	1092	X	4.23	1155	X	3.22	849	X	5.81	1232	Y	8.18	958	Y	6.65
7	1611	X	4.19	1432	Y	7.07	1177	X	5.14	849	Y	6.97	1514	X	5.90
8	1209	X	2.07	2710	Y	4.48	2710	Y	5.21	800	Y	6.40	1539	X	7.10
9	870	X	5.19	1439	X	8.32	835	Y	6.63	835	Y	7.95	1330	X	8.57
10	1789	X	7.71	1092	X	4.72	1206	X	5.94	1456	Y	4.27	1110	X	4.48
11	737	X	2.49	800	X	4.60	737	Y	3.22	2111	X	9.07	192	Y	8.64
12	300	X	1.97	323	X	9.09	1286	Y	3.70	789	X	6.92	760	X	6.13
13	1504	Y	0.83	870	Y	5.79	1817	X	5.65	1189	X	6.15	856	Y	8.30
14	1510	Y	1.41	1510	X	1.57	1533	X	1.99	1466	X	5.54	1344	Y	7.47
15	3317	X	1.96	3317	X	2.19	2651	X	7.95	2507	Y	2.89	2746	X	9.84
16	150	X	2.39	150	X	2.67	150	X	3.10	150	X	3.71	319	X	3.06
17	1472	X	2.37	2114	Y	0.87	1472	Y	3.07	1216	X	6.01	1492	X	1.19
18	1325	Y	9.03	1274	Y	8.05	1083	Y	4.39	862	X	5.40	1255	X	6.27
19	1503	X	0.57	3285	Y	4.52	1503	Y	0.74	1223	X	7.42	1262	X	5.25
20	2627	X	2.37	794	X	6.32	794	Y	7.33	1276	X	7.80	1106	Y	1.63

Ground motion sequence number from NGA database (Seq #), Selected component for response analysis (X/Y), Scale Factor (SF)